Chapter 2

Spatio-temporal evolution of seismic and aseismic slip on the Longitudinal Valley Fault, Taiwan

Marion Y. Thomas, Jean-Philippe Avouac, Johann Champenois and Jian-Cheng Lee

Abstract

The Longitudinal Valley Fault (LVF) in Eastern Taiwan is a high slip rate fault (about 5cm/yr) which exhibits both seismic and aseismic slip. Deformation of anthropogenic features shows that aseismic creep accounts for a significant fraction of fault slip near the surface whereas a fraction of the slip is also seismic since this fault has produced large earthquakes with five $M_w > 6.8$ events in 1951 and 2003. In this study, we analyze a dense set of geodetic and seismological data around the LVF including campaign-mode Global Positionnig System(GPS) measurements, times-series of daily solutions for continuous GPS stations (cGPS), leveling data and accelerometric records of the 2003 Chenkung earthquake. To enhance the spatial resolution provided by these data, we complement them with Interferometric Synthetic Aperture Radar (InSAR) measurements produced from a series of Advanced Land Observing Satellite (ALOS) images processed using a persistent scatterer (PS) technique. The combined dataset covers the entire LVF and spans the period from 1992 to 2010. We invert this data to infer the temporal evolution of fault slip at depth using the Principal Component Analysis-based Inversion Method (PCAIM). This technique allows the joint inversion of diverse data, taking the advantage of the spatial resolution given by the InSAR measurements and the temporal resolution afforded by the cGPS data. We find that (1) seismic slip during the 2003 Chengkung earthquake occurred on a fault patch which had remained partially locked in the interseismic period; (2) the seismic rupture propagated partially into a zone of shallow aseismic interseismic creep but failed to reach the surface; (3) that aseismic afterslip occurred around the area that ruptured seismically. We find consistency between geodetic and seismological constraints

on the partitioning between seismic and aseismic creep. About 80-90% of slip on the LVF in the 0-26 km seismogenic depth range is actually aseismic. We infer that the clay-rich Lichi Mélange is the key factor promoting aseismic creep at shallow depth.

2.1 Introduction

Fault slip can be either aseismic or seismic (i.e., radiating potentially damaging seismic waves). Geodetic and remote sensing techniques, combined with seismology, provide now the tools to quantify the partitioning between these two modes of slip and to investigate the various factors that control their spatial and temporal variations. A number of subduction zones studies have demonstrated, using these techniques, spatio-temporal variations of the mode of slip in the 0-50 km seismogenic depth range: fault slip might be dominantly aseismic at places, as a result of steady creep in the interseismic period or transient afterslip following large earthquakes, and dominantly seismic at others (*Heki et al.*, 1997; *Freymueller et al.*, 2000; *Wallace et al.*, 2004; *Cross and Freymueller*, 2007; *Fournier and Freymueller*, 2007; *Chlieh et al.*, 2008; *Perfettini et al.*, 2010; *Loveless and Meade*, 2011; *Miyazaki et al.*, 2011; *Evans et al.*, 2012). Similarly, strong spatial variations of slip mode have been documented on some continental faults (*Burgmann et al.*, 2000; *Titus et al.*, 2006; *Murray et al.*, 2001; *Jolivet et al.*, 2012; *Kaneko et al.*, 2013). However, how the partitioning between seismic and aseismic slip varies in time and space, and what are the factors governing this behavior (such as temperature, lithology, pore fluids), remain poorly understood questions. This is an important issue in seismotectonics since the seismic potential of any fault depends primarily on the partitioning between seismic and aseismic slip.

The objective of this study is to investigate this issue based on the modeling of the spatio-temporal evolution of slip on the Longitudinal Valley Fault (Figure 2.1). This fault runs parallel to the East coast of Taiwan and marks the suture zone between the continental margin of South China and the Luzon arc on the Philippine Sea Plate (*Lee et al.*, 2001; *Chang et al.*, 2009) (Figure 2.1a and 2.2). We chose to focus on this particular example as this fault is known to creep near the surface (*Angelier et al.*, 1997; *Lee et al.*, 1998, 2000, 2001, 2005; *Chang et al.*, 2009; *Champenois et al.*, 2012) but has also produced $M_w > 6.8$ earthquakes including 4 events in 1951 (*Shyu et al.*, 2007), and the Mw 6.8 Chengkung earthquake of 2003 (*Wu et al.*, 2006a; *Hsu et al.*, 2009a; *Mozziconacci et al.*, 2009). In addition the surface strain is well documented from campaign mode GPS (*Yu and Kuo*, 2001), continuously recording GPS stations (cGPS) of the Taiwan Earthquake center (http://gps.earth.sinica.edu.tw/), leveling data (*Ching et al.*, 2011; *Chen et al.*, 2012), creepmeters (*Lee et al.*, 2001, 2005; *Chang et al.*, 2009) and InSAR (*Hsu and Burgmann*, 2006; *Peyret et al.*, 2011; *Champenois et al.*, 2012). Finally, the slip rate on the Longitudinal Valley Fault is extremely fast, absorbing nearly half of the 9 cm/yr horizontal convergence rate between the Philippine Sea

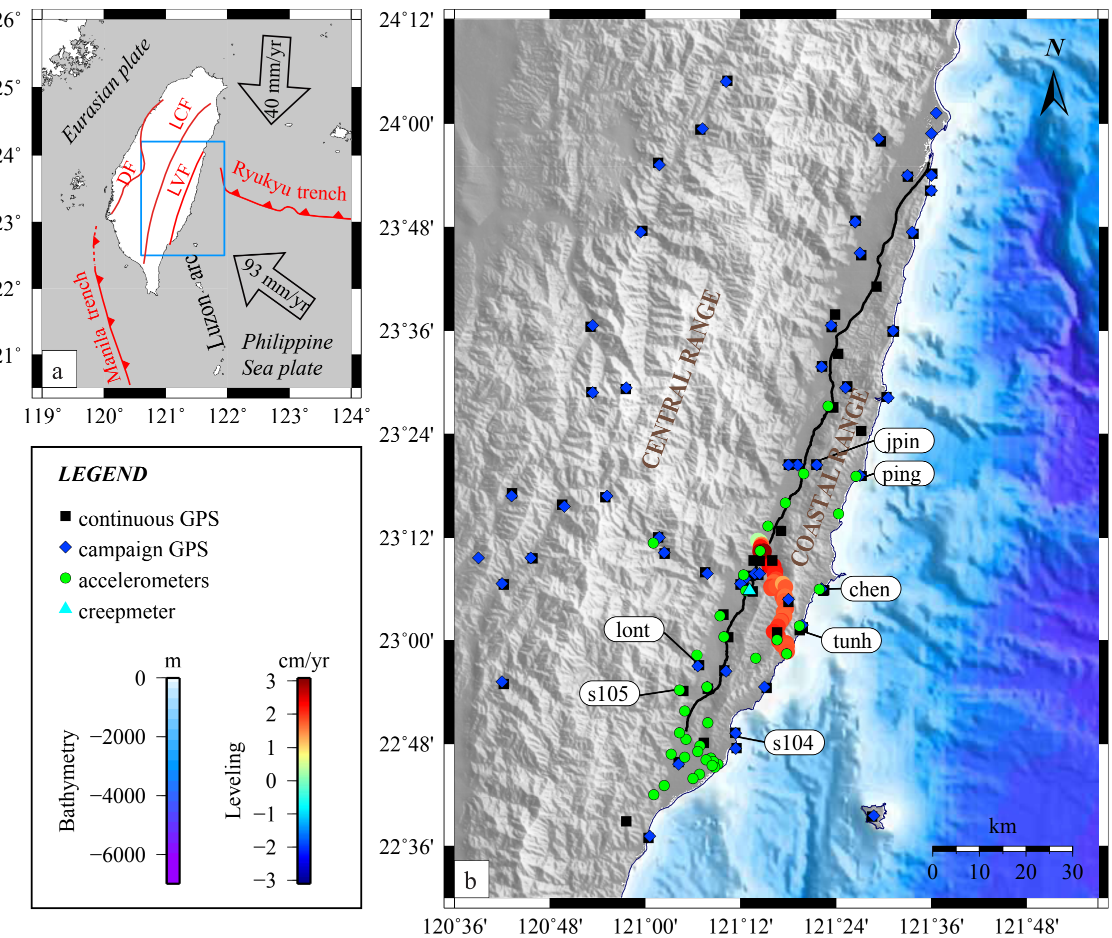

Figure 2.1: (a) Regional tectonic setting of the Longitudinal Valley Fault. Blue rectangle corresponds to the location of Figure 2.1b.DF-deformation front; LCF-Lishan-Chaochou Fault; LVF-Longitudinal Valley Fault.(b) Location of accelerometric, geodetic and leveling data used in this study. Black squared, blue diamonds, green circle and cyan triangle stand for the 67 permanent GPS stations(http://gps.earth.sinica.edu.tw/), the 38 accelerometers (*Wu et al.*, 2006a), the 45 campaign GPS sites (*Yu and Kuo*, 2001) and the creepmeter (*Chang et al.*, 2009; *Lee et al.*, 2005) respectively. We labeled the stations corresponding to the times series shown in Figure 2.4. Colored-scale circles show location of leveling measurements from 9/1/2007 to 31/20/2010 (*Chen et al.*, 2012).

Plate and South China (*Lee and Angelier*, 1993.; *Yu et al.*, 1997; *Hsu et al.*, 2003; *Shyu et al.*, 2006; *Huang et al.*, 2010)(Figure 2.1).

Hereafter, we first describe the dataset used in the study. It consists of a compilation of geodetic and remote-sensing data enhanced with new InSAR measurements. This dataset covers the period from 1992 to 2011. We next present our modeling results starting with the secular interseismic creep rates. We then discuss the coseismic slip distribution related to the Chengkung event, and finally we analyze the spatio-temporal variations of creep rates observed over the study period, in particular due to postseismic relaxation following the 2003 earthquake.

2.2 Data used in this study

In order to achieve the best possible resolution in our inversions of spatio-temporal variations of fault slip, we assembled all the data available on geodetic surface strain (Figure 2.1 and 2.2). We used in particular the data from the continuously recording GPS stations which were installed by the Central Weather Bureau and the Institute of Earth Sciences (http://gps.earth.sinica.edu.tw/), Academia Sinica of Taipei. We also compiled data from the literature. They include campaign GPS data (*Yu and Kuo*, 2001), accelerometric data (*Wu et al.*, 2006a), times-series of creepmeter measurements (*Lee et al.*, 2000, 2001, 2003, 2005; *Chang et al.*, 2009), leveling data (*Chen et al.*, 2012; *Ching et al.*, 2011) and the mean ground velocities measured from the Persistent Scatterer technique (PS) applied to PALSAR ALOS synthetic aperture radar (SAR) images covering the 2007-2010 period (*Champenois et al.*, 2012). These data cover the southern half of the Longitudinal Valley. We extended the existing SAR dataset with new measurements so as to cover the northern portion of the Longitudinal Valley (*Champenois*, 2011). The following sub-sections present these various data in more details.

There is also a leveling data set covering the whole island of Taiwan over the time period of 2000-2008 (*Ching et al.*, 2011). We use this dataset to check the consistency with the cumulative vertical displacements predicted by our model (see supplement Figure S11).

2.2.1 PS mean velocities from the ALOS PALSAR dataset

We used L-band PALSAR images (23.6 cm) provided by the ALOS satellite from the JAPAN Aerospace Exploration Agency (JAXA) to enhance the spatial resolution afforded by the GPS and leveling data and we supplement the results of *Champenois et al.* (2012) obtained on the southern portion of the Longitudinal Valley to achieve a full coverage of the study area (*Champenois*, 2011). We processed a 3 year long time-series, from 01/12/2007 to 09/07/2010, using the Persistent Scatterer (PS) approach (*Ferretti et al.*, 2001; *Hooper et al.*, 2007). The dataset consists of twelve SAR images which were acquired along the ascending path 444 every 3 months on average, except for a

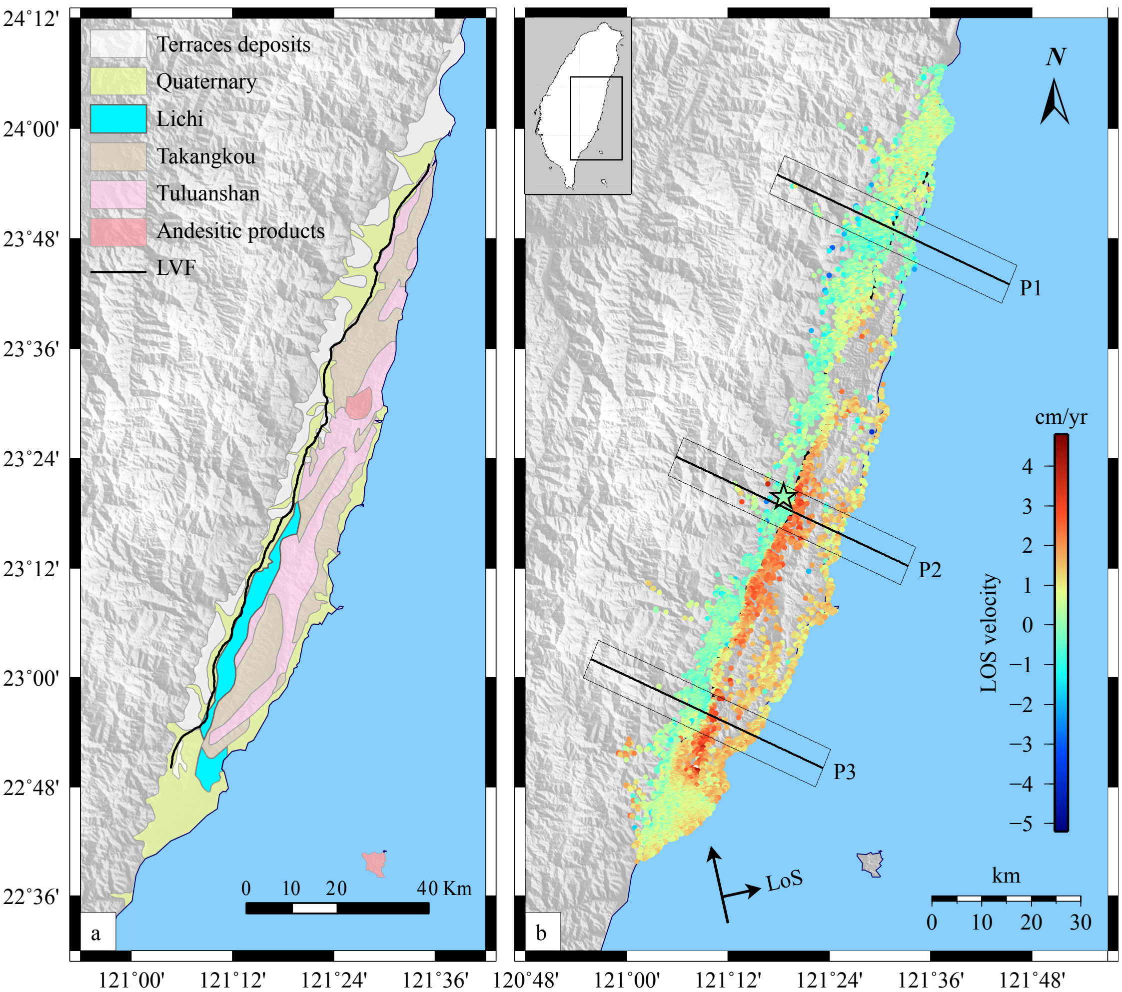

Figure 2.2: (a) Simplified geological map of eastern Taiwan. Coastal Range is composed of three accreted Mio-Pliocene volcanic islands (Tuluanshan formation), three remnants of Plio-Plesitocene forearc basins and intra-arc basins (Takangkou), and the Pliocene collision Lichi Mélange, which is related to the suturing of the subduction zone due to the collision between the Luzon arc (see Figure 2.1a) and the continental margin of South China (*Chang et al.*, 2000, 2001, 2009; *Huang et al.*, 2006b, 2008).(b) Mean line-of-sight (LoS) velocity (in cm/yr) around the Longitudinal Valley Fault derived from the Persistent Scatter technique applied to PALSAR ALOS data acquired between 1/29/2007 and 6/2/2010. Measurements from the southern portion (*Champenois et al.*, 2012) were complemented to cover the whole study area. Velocities are expressed relative to the mean velocity of a reference area, indicated by the black star. Black arrows show the ascending track direction and the LoS which has an incidence of about 35° on average (relative to the vertical). Boxes show location of swath profiles, P1, P2 and P3, plotted on Figure 2.3.

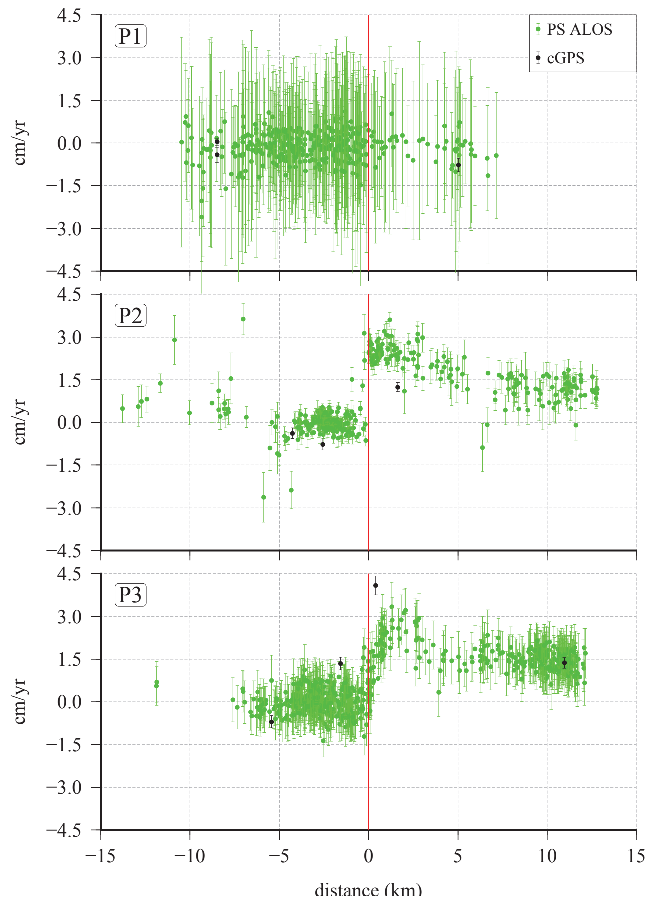

Figure 2.3: LoS velocities along swath profiles P1, P2 and P3. For location see Figure 2.2. Green dots show the PS mean velocity values, black dots show, for comparison, the velocities determined from cGPS times series, for the corresponding period and projected along the LoS. Red lines tag the location of the LVF at surface. PS ALOS Data display a net discontinuity across the fault for the profiles P2 and P3 whereas no jump is observed along profile P1. This discontinuity indicates clearly surface creep on the southern portion of the LVF as reported from field observations at a few sites (*Angelier et al.*, 1997; *Lee et al.*, 2005, 2006).

notable 9 months gap between January 2008 and October 2008. Because of the strong tropospheric effects affecting the time series we used these data to determine the mean LOS mean velocity over the 01/12/2007 to 09/07/2010 time period. Interferograms were generated using ROIPAC (*Rosen et al.*, 2004) with the 10/17/2008 acquisition chosen as the master image and a 40 m horizontal resolution digital elevation model (DEM) for topographic corrections (this national DEM was derived from aerial photogrammetry). We then applied the Stanford Method for Persistent Scatterers (StaMPS) (*Hooper et al.*, 2007). StaMPS uses both amplitude dispersion and phase stability to determine the pixels which can be considered as PS. No a-priori model of deformation is required, nevertheless it assumes that deformation, and consequently interferometric phase, is spatially correlated. The technique yielded a total of 147,737 PS with a density of about 120 - 140 PS per km^2. StaMPS allows estimating the mean ground velocities averaged over the time period covered by the time series, projected along the Line of Sight (LoS) of the satellite, at the location of each PS. Results are displayed in Figures 2.2 and 2.3. Mean velocities were computed with respect to a reference area, corresponding to the city of Rueisuei, near Yuli (black star on the map). Uncertainties estimated through the StaMPS method are of the order of 3-4 mm/yr on average (Table 2.2.1).

	σ_H	σ_V	σ
ALOS (*LoS*)			3.5 mm/yr
cGPS			
- daily position	4 mm	16 mm	
- secular rate	0.1 mm/yr	0.5 mm/yr	
- coseismic	1 mm	4 mm	
creepmeter			
- daily position			2 mm
- secular rate			0.1 mm/yr
campaign GPS	0.2 mm	0.4 mm	
Leveling$_a$		0 to 19 mm	
accelerometers	2.6 mm	1.8 mm	

Table 2.1: Summary of uncertainties associated to the various datasets used in this study (given at the 67% confidence level). (a) Leveling data are referred to the initial point in the survey. The uncertainty of elevation change measurement increases linearly as a function of distance from this point

The highest density of PS was retrieved in urban areas, in particular within the two largest cities in the Longitudinal Valley, Hualien in the North and Taitung in the South. For the same reason, we observe a greater density of PS inside the valley, where urbanization is the most developed, whereas PS are sparser in the Coastal Range, and mostly absent in the Central Range. The rugged topography and dense vegetation are most likely the reason for a lack of PS in those areas. The map of LoS velocities (positive toward the satellite) retrieved from this study shows a clear step in the velocity field along the LVF, south of 23°30 (Figure 2.2 and 2.3). This discontinuity is clear evidence of aseismic slip near the surface for the southern portion of the LVF. This observation is consistent with previously reported field observations of creep at a few sites (*Angelier et al.*, 1997; *Lee et al.*, 2005, 2006) and former InSAR studies (*Hsu and Burgmann*, 2006; *Peyret et al.*, 2011; *Champenois et al.*, 2012). We took advantage of the great spatial resolution to better define the surface trace of the fault in the South. In the North the ALOS PS measurements span the fault trace mapped by (*Shyu et al.*, 2005) but show no clear discontinuity (at the detection level of the technique which we estimate to about 2 mm/yr at the 67% confidence level) (Table 2.2.1), suggesting the shallow portion of the fault has remained locked over the 2007-2010 period.

2.2.2 Continuous GPS stations

A remarkable network of cGPS stations has been deployed in Taiwan. For the purpose of this study, we used times series data from 67 stations spanning the Longitudinal Valley, the Coastal Range, the western part of the Central Range and the Ludao island (Figure 2.1) (http://gps.earth.sinica.edu.tw/). Times series starts on 1/1/1994 for the earliest stations. We analyzed data collected until 11/26/2010 (Figure 2.4).

The dominant sources of signal over this time period are the interseismic loading, the coseismic and postseismic displacements due to the 2003 Mw 6.8 Chenkung earthquake (*Chen et al.*, 2006; *Lee et al.*, 2006; *Wu et al.*, 2006a; *Ching et al.*, 2007; *Hu et al.*, 2007; *Kuochen et al.*, 2007; *Savage*, 2007; *Wu and Wu*, 2007; *Cheng et al.*, 2009; *Hsu et al.*, 2009a; *Huang et al.*, 2009; *Mozziconacci et al.*, 2009). The southernmost stations in the Longitudinal Valley have also recorded displacements due to the 2006 Mw6.1 Peinan earthquake (*Wu et al.*, 2006b; *Chen et al.*, 2009). This earthquake did not take place on the LVF but on a fault bounding the Central Range (*Wu et al.*, 2006b; *Chen et al.*, 2009). Therefore, for the purpose of this study, we corrected the GPS times series for the effect of the 2006 Peinan earthquake and its subsequent postseismic relaxation, by solving the following equation:

$$\begin{aligned} u^i(t) = u_0^i + v^i(t) + \sum_j h_j^i \mathcal{H}(t - t_k) \\ + \sum_k r_k^i \mathcal{H}(t - t_k) \log(1 + (t - t_k)/\tau) \\ + \sum_p \left(s_p^i \sin\left(\frac{2\pi t}{T_p}\right) + c_p^i \cos\left(\frac{2\pi t}{T_p}\right)\right), \end{aligned} \tag{2.1}$$

where i = (north, east, up), u_0 is a constant offset, $v(t)$ correspond to the secular velocity, $\mathcal{H}$ is a Heaviside step function standing for coseismic displacement, t_k is the time at which the step occurs and the Heaviside step function multiply by the logarithmic function follows the postseismic

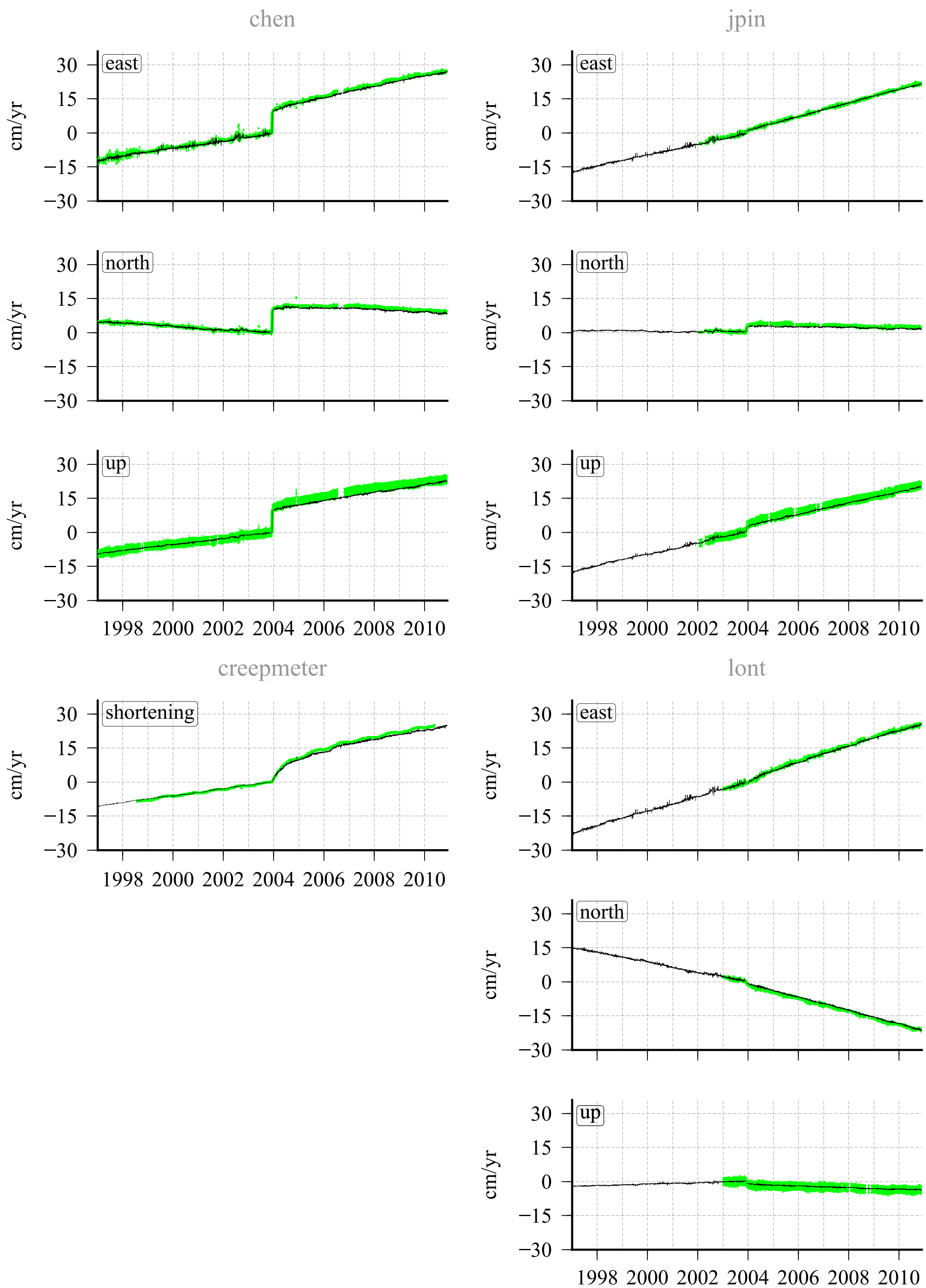
chen
jpin
creepmeter
lont
east
north
up
shortening
cm/yr
30
15
0
−15
−30
1998 2000 2002 2004 2006 2008 2010

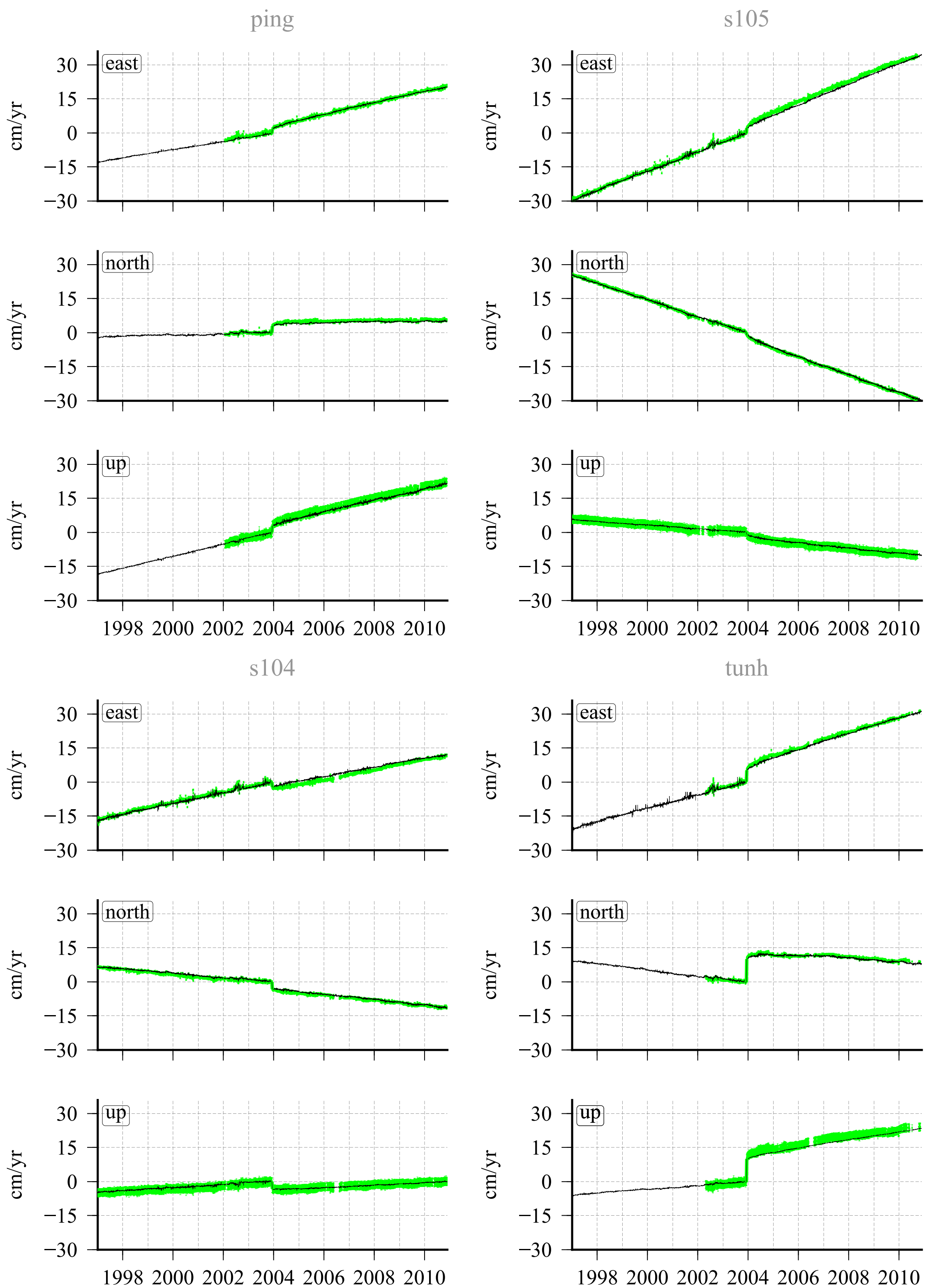
ping
s105
s104
tunh
east
north
up
cm/yr
30
15
0
−15
−30
1998
2000
2002
2004
2006
2008
2010

Figure 2.4: Plots of times series recorded at CGPS stations chen, jpin, lont, ping, s104, s105, tunh (http://gps.earth.sinica.edu.tw) and creepmeter measurements (*Chang et al.*, 2009; *Lee et al.*, 2005). See Figure 2.1 for location. We show a selection of stations with long time records and surrounding the coseismic and postseismic area. See supplements for other times series (Figures S1, S2 and S3). Blue dots with 1-sigma errors bars represents the original dataset. Predictions from the inversion of Coseismic slip and PCAIM inversions of preseismic and postseismic periods are plotted in black To facilitate the comparison we have corrected the model predictions for the mean residual velocities over the pre and post-seismic period represented in Figures 2.17 and 2.19.

relaxation with τ, the characteristic time constant. To model annual variations in equation (2.1) we used sine waves of period T_p. We explored two periods: one year and half a year. The linear parameters u_0^i, v^i, h_j^i, r_k^i, s_p^i and c_p^i are estimated through a standard least-squares inversion. Artificial steps due to maintenance operations, small local earthquakes or equipment malfunction might also affect the signal. We removed them from the times series by applying the same process (equation 2.1). Based on the residuals obtained from fitting the corrected time series with a linear regression (equation 2.1), we estimate the uncertainties on daily positions to be about 4 mm for the East and the North component and 16 mm for the vertical components (Table 2.2.1).

2.2.3 Creepmeter data

Creep on the Chihshang segment of the LVF has been measured daily over the last 15 years thanks to a network of creepmeters (*Lee et al.*, 2000, 2001, 2003, 2005; *Chang et al.*, 2009). We used data from 7/26/1998 to 5/24/2010 from the three creepmeters installed at Chinyuan site (Figure 2.1) but did not include the records from the Tapo site because gravity driven slumping is thought to interfere with fault-slip at this site (*Lee et al.*, 2003). Creepmeters have been set up across the three major splay faults within a 120 m-wide deformation zone. Each creepmeter provides a scalar measurement of the horizontal shortening along the baseline of the instrument ($N113°$, $N156°$ and $N164°$). We projected and sum the time series along the direction of maximum shortening ($N146°$) defined by trilateration method and GPS interseismic vectors at the same site (*Angelier et al.*, 1997; *Lee et al.*, 2006).

No detectable coseismic slip occurred at the surface during the 2003 Chengkung earthquake. By contrast, accelerated creep (*i.e.*, postseismic creep) was observed during the year following the event (Figure 2.4). All three creepmeters at Chinyuan site show strong seasonal variation of fault creep with fast creep during wet season and quiescence during the dry season. This behavior is interpreted to result from pore-pressure variations case by rainfall, as suggested by the correlation with piezometric measurements in a local well (Chang et al, 2009). Based on the residuals obtained from fitting the time series with a linear regression (equation 2.1), we estimate the uncertainty on the individual creepmeter measurements to be 2 mm at the 67% confidence level (Table 2.2.1).

2.2.4 Campaign GPS measurements and secular GPS velocity field.

Annual GPS survey at 45 campaign sites have been conducted across the Longitudinal Valley between 1992 and 1999 (*Yu and Kuo*, 2001) (Figure 2.1). Estimated uncertainties based on (*Yu and Kuo*, 2001) is 0.2 mm for the East and the North component and 0.4 mm for the vertical components (Table 2.2.1). These velocities were combined with the secular velocities at the continuous GPS stations were also computed based on equation (2.1). The corresponding uncertainties are 0.1 mm/yr for the northern and eastern components and 0.5 mm/yr for the vertical (Table 2.2.1).

2.2.5 Leveling data

We used vertical displacements derived from leveling survey in southern part of the Coastal Range (Figure 2.1). Those measurement were acquired on an annual basis between 9/1/2007 and 31/20/2010 along a leveling line crossing the Chihshang segment of the Longitudinal Valley fault (*Chen et al.*, 2012). We used these data to estimate the average vertical rates (relative to the first station along the leveling line) over the 9/1/2007 and 31/20/2010 period. Uncertainties varies from the initial reference point (0 mm) up to 19 mm for the last point (Table 2.2.1).

2.2.6 Accelerometric data

In order to constrain coseismic slip due to the 2003 Mw6.8 Chengkung earthquake, we used the static displacements measured from the offsets in the cGPS records together with the static displacements determined by Wu et al. (*Wu et al.*, 2006a; *Hu et al.*, 2007) from the accelerometric measurements recorded at 38 stations from the TSMIP network (Figure 2.1). TSMIP stations, operating under low-gain mode, sample the signal at 200 Hz (*Wu et al.*, 2006a). Uncertainties were inferred to be 2.9 mm for the horizontal components and 1.9 mm for the vertical (*Wu et al.*, 2006a) (Table 2.2.1).

2.3 Modeling approach and assumptions

The dataset presented above was used to estimate the time-evolution of slip on the LVF. We assume that that the medium surrounding the fault is behaving elastically and apply the *Okada* (1985) semi analytical solution to relate slip at depth to surface displacement. This solution assumes an elastic half space. Heterogeneities of elastic properties and topographic effects are neglected. This approach is known to provide a good first order approximation in general (*Segall*, 2010). This approach requires some model of the fault geometry at depth and some inversion procedure.

2.3.1 Fault geometry and forward modeling

We defined a 3-D fault geometry based on the location of aftershocks at depth of the Chengkung event (*Kuochen et al.*, 2007; *Wu et al.*, 2007, 2008b) and surface trace of the LVF determined from the discontinuity in PS ALOS velocity field (Figure 2.2) and the geomorphologic expression of the fault for the northern part (*Shyu et al.*, 2005) (Figure 2.5). Both, the relocated seismicity as well as local tomographic results (*Kuochen et al.*, 2007; *Wu et al.*, 2007, 2008b) suggest the LVF is a listric fault with a dip angle decreasing gradually from about 62° at shallow depth (0-14m) to 19° at 27 km depth and thereafter. This geometry is relatively well constrained for the central to southern portion of the LVF, because of the intense aftershocks activity following the Chengkung earthquake. We assume that the same listric geometry holds for the northern portion of the LVF although we have no direct constraints there. Fault is subdivided in 44 x 15, 3.16 x 3.16 km^2 patches. The fault extends over about 140 km along strike (the length of the Longitudinal Valley) and about 47 km along dip.

Assuming a linear purely elastic half-space, displacements at surface are related to the fault slip distribution through a Fredholm integral equation of the first kind, which, if we use k measurements and discretize the fault plane in l patches, gives in the matrix from:

$$\mathbf{d} = \mathbf{G}\mathbf{m}, \tag{2.2}$$

where $\mathbf{d}$ is the input data vector, $\mathbf{G}$ is the kxl Green's functions matrix that relates slip at depth and surface displacements, and $\mathbf{m}$ is the vector of parameters we are solving for, i.e. strike-slip and dip-slip components of the slip vector. For an elastic half-space the Green functions depend only on the Poisson ratio which is fixed to 0.25. The rigidity modulus is fixed to as standard value of 30 GPa and used only to convert slip potency (integral of slip over fault area) to moment (expressed in N.m).

2.3.2 Inversion procedure

The slip distribution needed to account for the observed surface displacements $\mathbf{d}$, is solved through a standard linear inversion. In order to take into account the uncertainties on the measurements we normalize the data using C_d, the data covariance matrix. This procedure allows combining data with different noise characteristics, such as GPS and InSAR obervations with appropriate relative weighting. Equation (2.2) then becomes:

$$\mathbf{C_d}^{-1}\mathbf{d} = \mathbf{d}^* = \mathbf{C_d}^{-1}\mathbf{G}\mathbf{m} = \mathbf{G}^*\mathbf{m}. \tag{2.3}$$

This is the equation that we seek to solve for fault slip, $\mathbf{m}$. In principle a linear inversion of that equation provides the solution which minimized the weighted rms of the difference between the observed and predicted displacement, with the weighting of each data point being determined by its uncertainty. This is equivalent to minimizing a reduced Chi-squared criterion defined as:

$$\chi^2_{red}(\mathbf{m}) = 1/n \parallel \mathbf{G}^*\mathbf{m} - \mathbf{d}^* \parallel^2, \tag{2.4}$$

where n is the number of data point.

However the inversions described below are poorly constrained due to the large number of unknowns (1320) and trade-offs among model parameters. To regularize the inversion, we impose fault slip distribution to be smooth. Following an approach suggested by *Lohman* (2004), we weight the constraint put on smoothing according to local resolution of the inversion. Therefore, fault slip is retrieved by minimizing some combination of the model ability to fit the data and the penalty imposed on the roughness of the slip distribution which is quantified from its Laplacian:

$$\phi_d = \parallel \mathbf{G}^*\mathbf{m} - \mathbf{d}^* \parallel^2 + \frac{1}{\lambda} \parallel \mathbf{S\Lambda m} \parallel^2, \tag{2.5}$$

where $\mathbf{\Lambda}$ is the Laplacian matrix, $\mathbf{S}$ is a diagonal smoothing shape matrix that weight each row of $\mathbf{\Lambda}$ and λ define the weight attributed to the penalty. $\mathbf{S}$ is defined as the inverse of the width of the best-fitting gaussian curve to each row of the resolution matrix (see supplement from *Ader et al.* (2012) for details). Consequently, well resolved patch have small or no smoothing applied, whereas, poorly resolved mesh grids are strongly smoothed with their neighbourhood.

Figure 2.6 illustrates the resolution for the various inversions described below. The resolution is expressed here in terms of the characteristic size of smallest inhomegeneities of coupling which could in principle be resolved given the spatial distribution and the uncertainties of the measurements. For each case we take into account the distribution of data and their uncertainties and plot, at the location of each cell of the fault model, the width of the best-fitting gaussian curve to each row of the resolution matrix. This is in effect representing the width of the equivalent Gaussian distribution that is retrieved if one inverse the displacements predicted for a unit slip at the considered cell. These maps show that, past the coastline, the resolution on fault slip at depth becomes quite poor as expected given the absence of any offshore constraints except for the cGPS station on Ludao island (Figure 2.1). Features smaller than about 10 km cannot in principle be resolved there. Updip of the coastline the resolution is generally better than about 5 km.

To illustrate the resolution power of our inversions, we show in Figure 2.7 the result of the inversion of a synthetic source model. The input is a rectangular source with a uniform slip or 1 m. The location and size of the source was chosen so that this source is comparable to that of the M_w 6.8 earthquake. Synthetic displacements were computed at the location of the GPS and

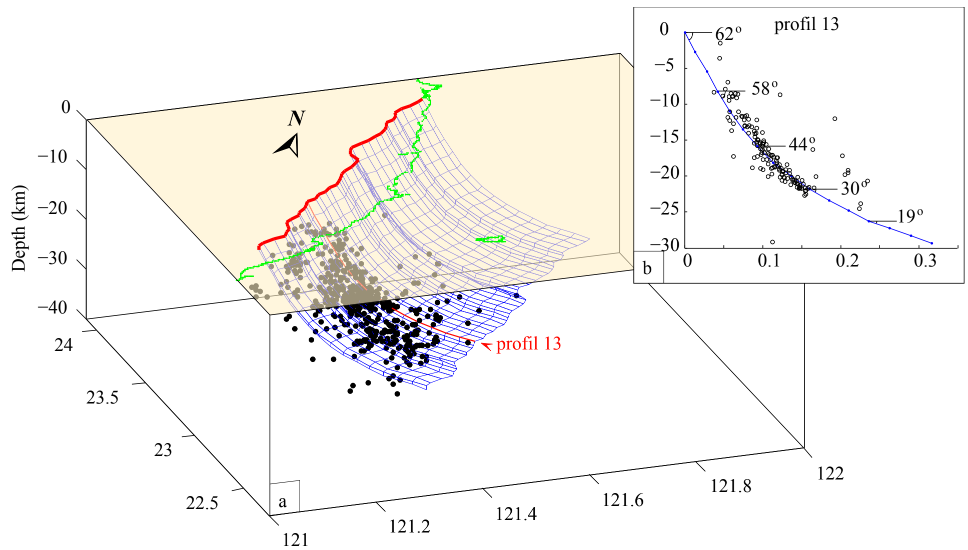

Figure 2.5: (a) 3-D fault geometry (blue grid) determined from the surface fault trace (red line) and relocated seismicity(black dots) for events of $M_w \geq 2.5$ (*Wu et al.*, 2008a). The geometry at depth is well constrained only in the Chengkung earthquake area due to the intense afterschocks activity. (b) Profile shows the variation of dip angle with depth. Black dots corresponds to seismic events.

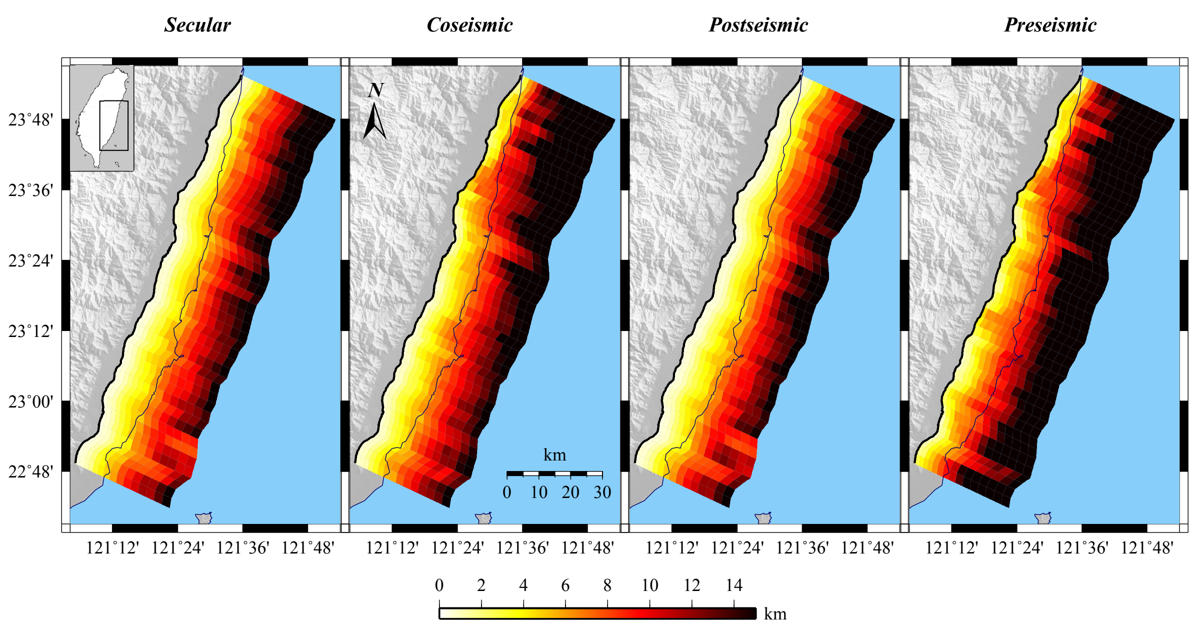

Figure 2.6: Resolution of the various inversions described in this study. The width of the best-fitting gaussian curve to each row of the resolution matrix is plotted at the location of each cell of the fault model. This is in effect representing the width of the equivalent Gaussian distribution that is retrieved if one inverse the displacements predicted for a unit slip at the considered cell.

accelerometric stations and were assigned the same uncertainties as the original observations.

2.3.3 Block model correction

Before any inversion for fault slip rate with depth, the surface displacements must first be referred to a local reference frame. In effect, we need to determine the long term motion of the Coastal Range and Central Range which are bounding the Longitudinal Valley Fault to the east and west respectively. As is customary in plate tectonics or continental deformation studies, we use the Euler pole formalism to describe the long term motion of the Coastal Range (CoR) and Central Range (CeR) blocks. Given that all the GPS stations are closed to the LVF, it is not possible to determine these Euler poles reliably without taking into account interseismic strain. We therefore first determine jointly the secular pattern of fault slip (time-averaged fault slip over the study period) and the Euler poles of the CeR and CoR blocks relative to ITRF2005 (section 2.4). Then we infer coseismic slip due to the Chenkung earthquake. Both coseismic and secular interseismic model are determined simply from solving equation (2.5) in which $\mathbf{d}$ represents the surface displacements. To retrieve the temporal variations of fault slip for the period preceding and following the 2003 event, we used the PCAIM method (*Kositsky and Avouac*, 2010), explained in more details in section 2.6.1.

2.4 Secular Interseismic Model

2.4.1 Data used

We determine in this section the secular Model of fault slip rate on the LVF, in the interseismic period. For that purpose, we use GPS campaign measurements, leveling data, PS ALOS mean velocity and secular velocities determined with the continuous GPS and creepmeters time-series (as determined from least squares fitting of the time series with equation (2.1)). The leveling and ALOS datasets were acquired more than three years after the 2003 Chengkung earthquake. According to the GPS and creepmeter postseismic relaxation was mostly over by this time. Therefore, these data are incorporated in the secular inversion, which improves significantly the spatial resolution. Uncertainties assigned to these datasets are displayed in Table 2.2.1.

2.4.2 Euler pole correction

In order to get a secular model of slip on the LVF we need to evaluate the long term motion of the CoR and CeR blocks. Evidence for active thrusting offshore the eastern coast of Taiwan (*Malavieille et al.*, 2002; *Huang et al.*, 2010) dismisses the CoR block as part of the Philippine Sea Plate. In addition, the Philippine Sea Plate motion is very poorly constrained as this plate is bounded only by subduction zone and the few GPS sites on this plate might be affected by plate-boundary strain.

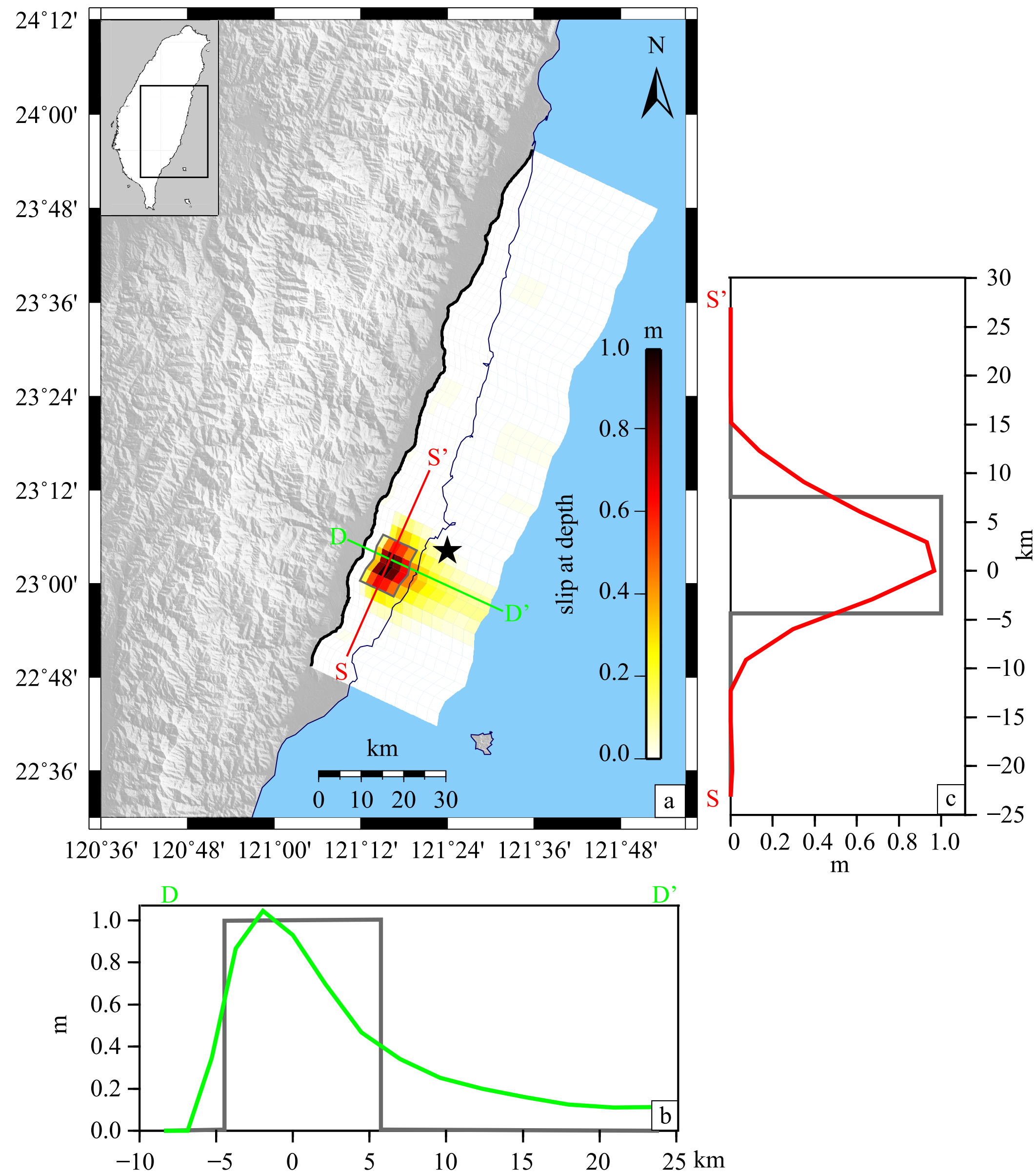

Figure 2.7: Resolution test. The input is theoretical displacements computed for a rectangular source (black box) with a uniform slip or 1m. The location and size of the source was chosen so that this source be comparable to that of the Mw 6.8 earthquake. Synthetic displacements were computed at the location of the GPS and accelerometric stations and were assigned the same uncertainties as the original observations. The left and bottom panels show the input and inverted slip distribution along strike (SS) and along dip (DD) respectively. Locations of profiles are reported in the map view.

We therefore need to determine the secular motion of that block. This requires to take into account the interseismic strain associated with the LVF since all the geodetic data are located less than ~ 20 km away from the fault. Similarly, the CeR blocks is not fixed with respect to South China due to active thrusting along the western foothills of Taiwan (*Hsu et al.*, 2003) and none of the GPS data can reliably be considered to represent the long term motion of the CeR block. Therefore, we use a simple 2 steps procedure to evaluate the Euler poles describing the long term motion of these two blocks, with the Philippine Sea Plate chosen as a reference. We first express the GPS velocities with respect to the Philippine Sea Plate by using the Euler pole (ITRF-Ph) computed by *DeMets et al.* (2010), (Table 2.4.2 and Figure 2.8).

Then, using the backslip modeling approach (*Savage*, 1983) we invert for slip at depth using the campaign GPS data and the secular velocities derived from the continuous GPS times series, for stations East of the LVF. This model is then used to predict the GPS velocities at stations in the footwall (West of LVF) to further compare them with the secular velocities measured at those locations. If the LVF is assumed to be the only source of strain in the study area, then the residuals represent the long term motion of the footwall with respect to the Philippe Sea plate. Residuals for stations in the Central Range are then used to compute the Euler pole of the CeR block from a linear least-squares inversion (CeR/Ph pole in Table 2.4.2 and Figure 2.8). Next we use the CeR/Ph Euler pole to express the secular velocities of the western stations in the local CeR reference frame. These data are now inverted for the coupling on the LVF using the backslip approach. Similarly to the previous step, we predict displacements at stations lying on the eastern side of the LVF and compute the residuals with the secular velocities at those sites, expressed in the CeR reference frame. We can now use these residuals to compute an Euler pole describing the motion of the CoR relative to CeR (see CeR/CoR pole in Table 2.4.2 and Figure 2.8). It is now possible to express the geodetic data in either the CeR or CoR reference frame, and predict the long term slip on the LVF fault needed to accommodate the relative block motion between the Central Range and Coastal Range (Figure 2.9). The computation assumes that the blocks behave rigidly in the long term. This is only a first order approximation as the LVF is not strictly planar.

	Ph/ITRF	CeR/Ph	CeR/CoR	CoR/Ph
Latitude	47.1	32.15	-23.34	-19.42
Longitude	150.4	133.30	-54.93	-58.11
$\Omega(^\circ/\text{Myr})$	-0.9251	-2.1351	7.0154	-4.94

Table 2.2: Location of axis and angular rotation rates of Euler poles used to describe the relative motions of the Philippine Sea Plate (Ph), Central Range block (CeR), and Coastal Range block (CoR).

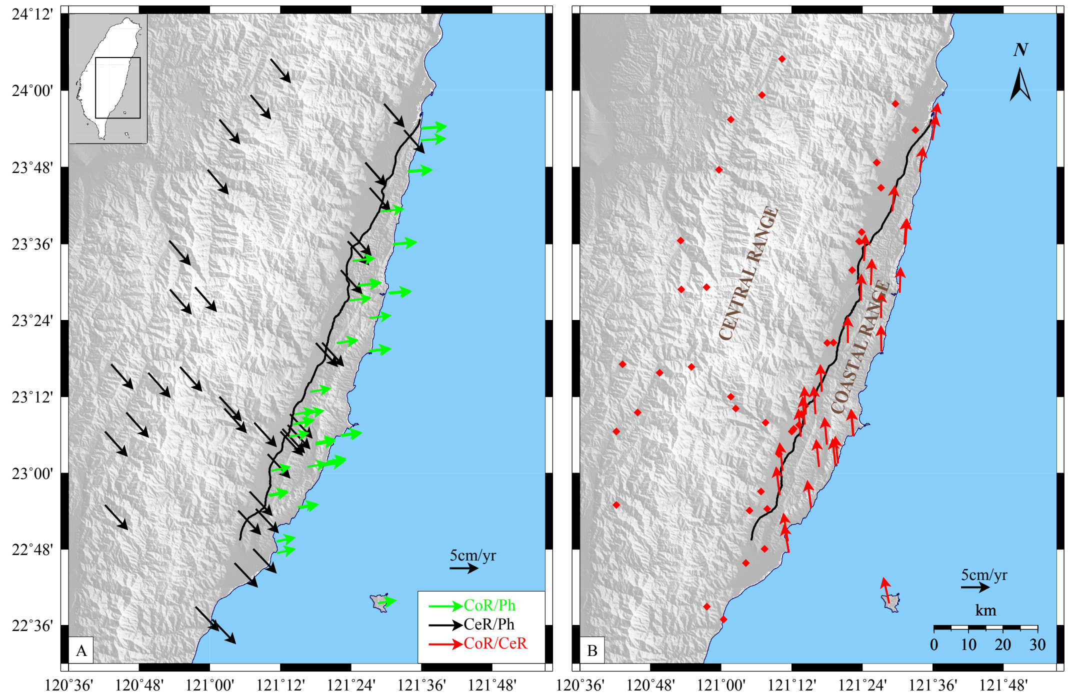

Figure 2.8: (a) Secular motion of the Central Range (black arrows) and Coastal Range (green arrows) blocks relative to the Philippine Sea Plate as defined by Philippine/ITRF (*DeMets et al.*, 2010). (b) Secular motion of the Coastal Range relative to the Central Range. Pole parameters are listed in Table 2.4.2.

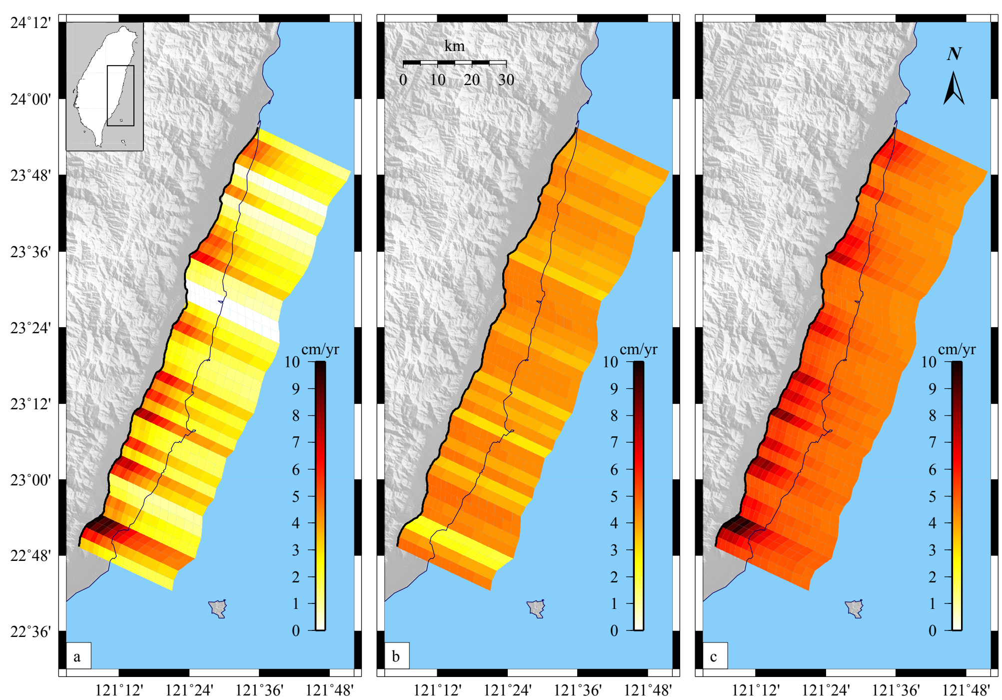

Figure 2.9: Dip-slip component (a), strike-slip component(b) and magnitude (c) of long term slip rate on the LVF predicted from the secular relative motion between the Central Range and Coastal Range. This computation is based on the CoR/CeR pole listed in Table 2.4.2.

2.4.3 Interseismic slip and coupling on the LVF

We now use the complete dataset of InSAR, GPS and leveling measurements to determine the time-averaged pattern of slip rate on the LVF in the interseismic period. We assume that the deeper continuation of the fault is slipping at the long term slip rate imposed by the relative block motion between the Central Range and Coastal Range, as predicted by the CeR/CoR Euler pole established in the previous section. Because of the very limited sensitivity of our data to slip at depth, we limit the inversion to the fault portion shallower than 26 km (corresponding to 15 cells of our gridded fault along the downdip direction). We first predict the theoretical displacements at stations by assuming that the fault is fully locked from the surface to a depth of 26 km. To compute such model we use again the backslip approach (*Savage*, 1983). The CeR/CoR pole Euler pole characterize the long-term surface velocities and the backslip model is added to account for locking of the LVF down to a 26 km depth. We then substract the velocities predicted by this model from the measured velocities. These residual must contain the signal due to creep on the LVF. We can now inverse the residuals to get the spatial variation of secular slip rate on the LVF in the 0-26 km depth range of our model. We apply this procedure to all the data, including continuous and campaign GPS data, leveling measurements and PS ALOS mean velocities. The slip rate distribution obtained from this inversion, as well as the comparison between the model predictions and the observations are plotted in Figures 2.10(a), 2.11, 2.12 and 2.13. This model highlights the sections of the fault which are creeping from the ones which remain locked. As previously recognized, the southern portion of the fault is creeping near the surface (*Angelier et al.*, 1997; *Lee et al.*, 2000, 2001, 2003, 2005; *Hsu and Burgmann*, 2006; *Lee et al.*, 2006; *Chang et al.*, 2009; *Cheng et al.*, 2009; *Hsu et al.*, 2009b; *Huang et al.*, 2010; *Peyret et al.*, 2011; *Champenois et al.*, 2012; *Chen et al.*, 2012; *Chuang et al.*, 2012). Our study highlights that, on the contrary, the northern part is mostly locked. Pattern at depth is more complex, with areas creeping at high rate, connecting the deeper and the upper part, while others seem to be locked or partially locked. Moreover, epicenters of historical earthquakes on the LVF (1938,1951,2003) (*Chung et al.*, 2008) seem to correlate with the location of partially locked patches (Figure 2.10b).

We can next estimate the interseismic coupling (ISC) which quantifies the degrees of locking of the fault. ISC is defined as the ratio of slip deficit divided by the long term slip rate.

$$ISC = 1 - \frac{V_{int}(x)}{V_{pl}(x)}, \tag{2.6}$$

where V_{pl} is the long-term slip rate on the fault and V_{int}, the slip rate during the interseismic period. In principle, if no transient events occurs during the time period considered to compute V_{int}, ISC values should be between 0 and 1. If $ISC = 1$, then patch is fully locked, accumulating stress to be released during transient slip events (earthquakes or aseismic slow slip events for example). On the

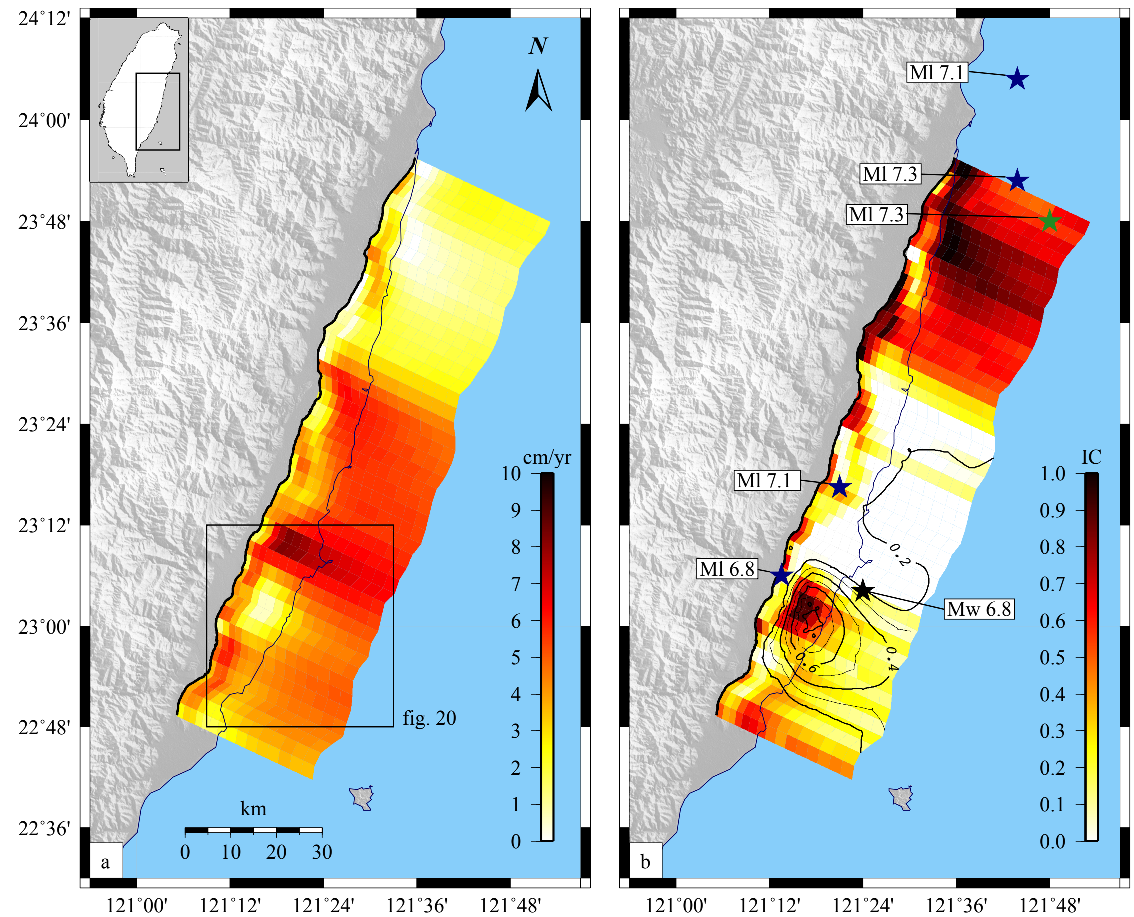

Figure 2.10: Secular interseismic model. (a) Slip rate distribution derived from the inversion of campaign GPS data, secular interseismic velocities inferred at cGPS stations, creepmeter secular rate, leveling data and PS ALOS mean velocities. Black rectangle shows locations of the map view displayed in Figure 2.20. (b) Interseismic coupling (ISC) distribution derived from the interseismic slip rate distribution shown in (a). ISC quantifies the degrees of locking of the LVF fault. If $ISC = 1$, then patch is fully locked, whereas $ISC = 0$ means that the patch is creeping at the long-term slip rate. Black, green and blue stars indicate the epicenter of the 2003 Chengkung earthquake, the 1938 earthquake and the 1951 earthquakes sequence respectively (*Chung et al.*, 2008). Back curves show contour lines of coseismic slip distribution for the 2003 Mw 6.8 Chengkung Earthquake (Figure 2.14).

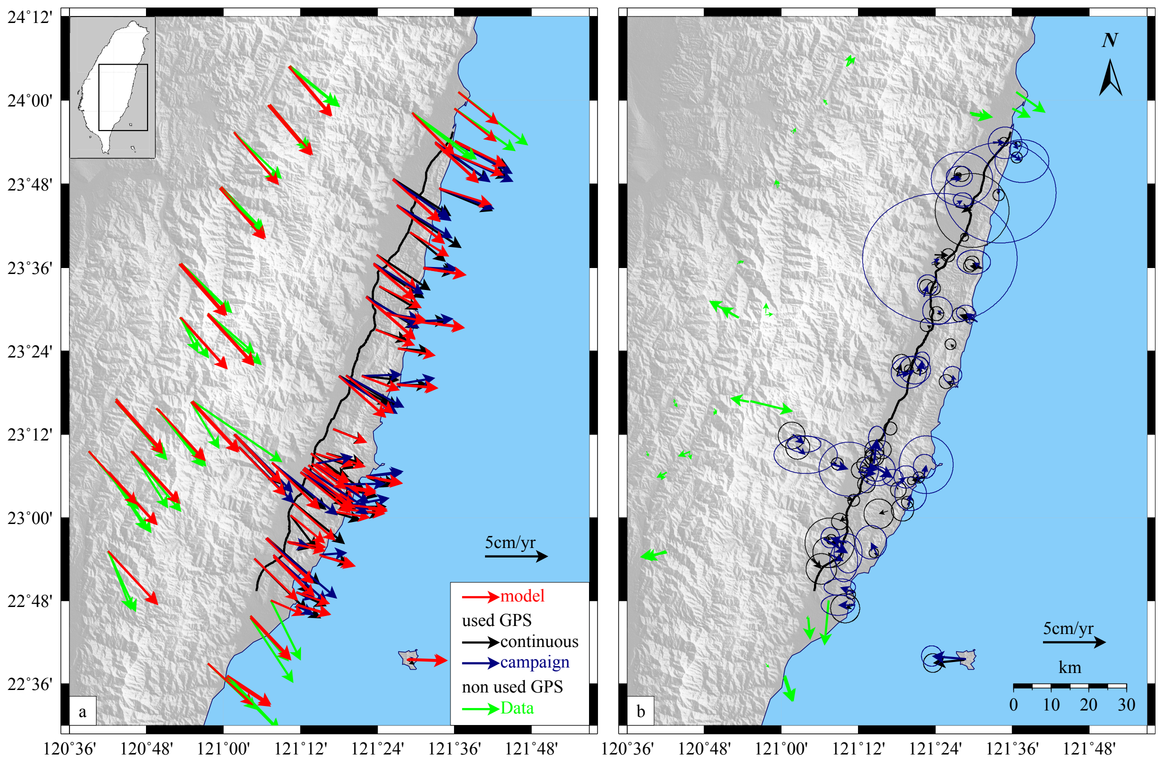

Figure 2.11: Interseismic coupling model, fit to geodetic data. (a) Comparison between observed and predicted horizontal velocities. The reference frame is the Philippine Sea Plate. The GPS data used in this inversion are plotted respectively as dark blue and black arrows for the campaign and continuous GPS measurements. Green arrows stand for the GPS stations that were not used in the inversion but which are plotted for reference. Predictions from the interseimic coupling model are displayed in red. (b) Residuals from the inversion with corresponding error ellipses. Same color attributions as in (a).

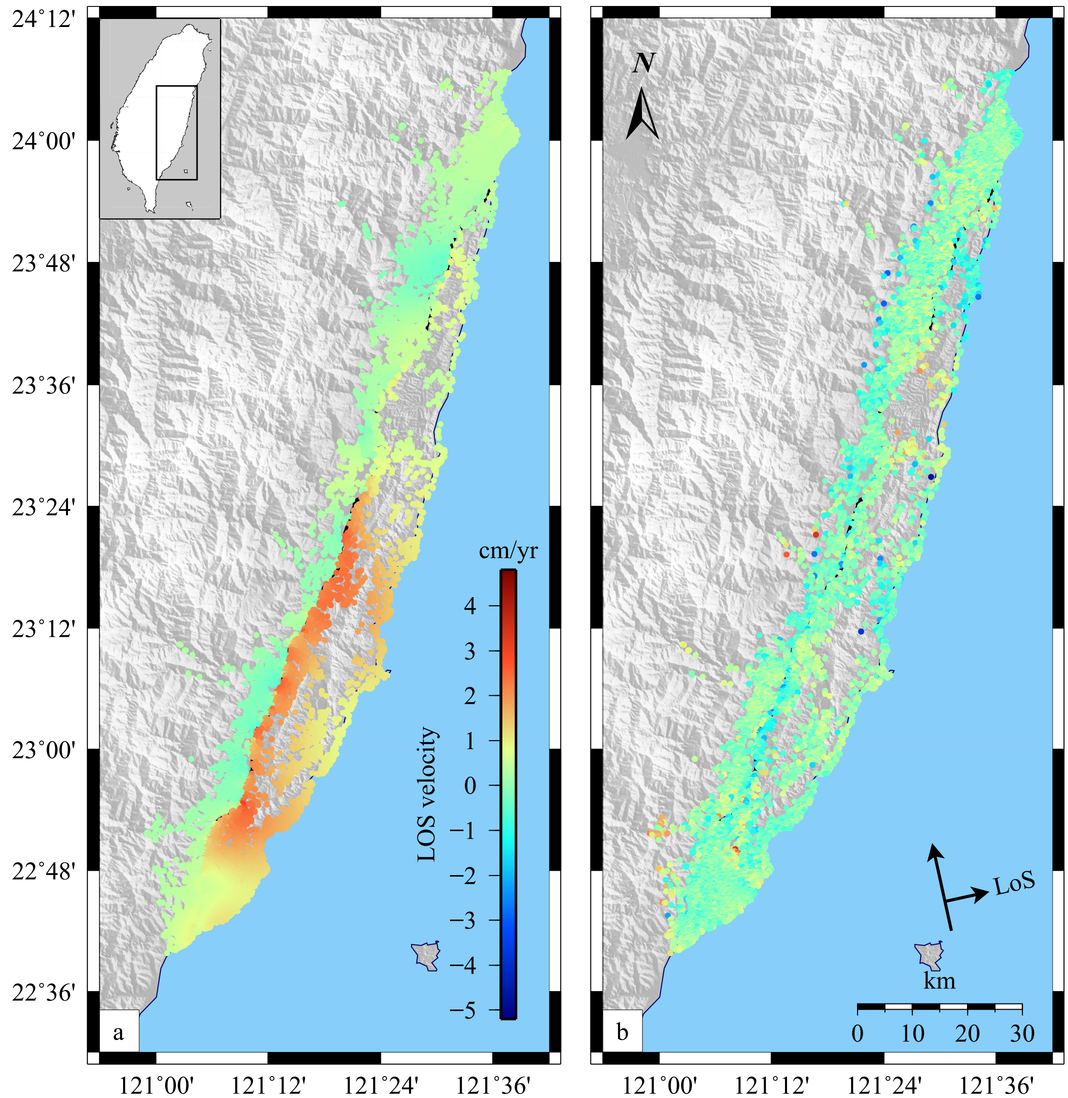

Figure 2.12: Interseismic coupling model, fit to PS ALOS mean velocity. (a) Line of Sight velocities predicted from the secular interseismic model. For comparison with observations see figure 2.2. (b) Residuals from the inversion with same color scale as in (a).

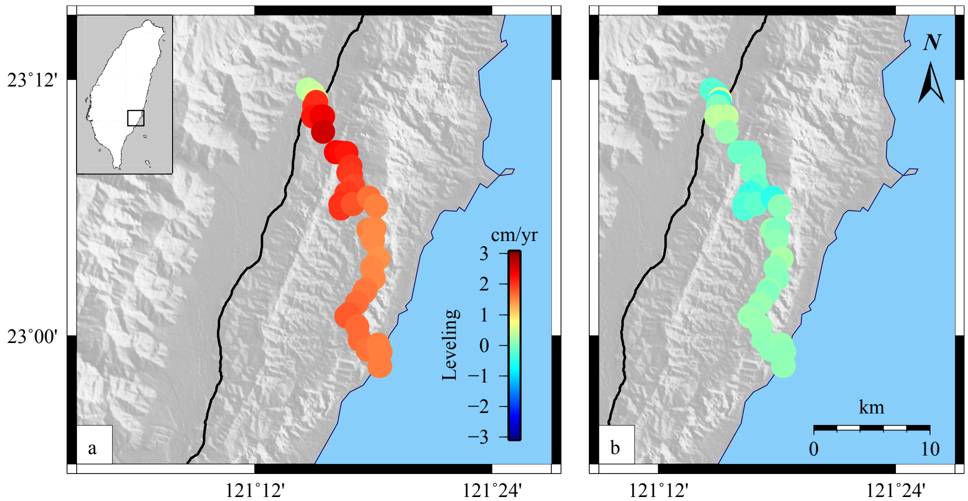

Figure 2.13: Interseismic coupling model, fit to leveling data. (a) Vertical velocities predicted from the secular interseismic model. See Figure 2.1 for corresponding observations. (b) Residuals from the inversion with same color scale as in (a).

contrary, $ISC = 0$ means that the patch is creeping at long-term slip rate. To compute the ISC on the LVF we divide the slip rates derived from the inversion of surface strain with the long term slip rate predicted by the CeR/CoR Euler pole (Figure 2.9). The inferred distribution of ISC is dispayed in Figure 2.10b.

2.5 Source model of the 2003 Chengkung earthquake

We present here our determination of the slip distribution related to the Chengkung earthquake. This event, which occurred on December 10^{th} 2003, ruptured the south-eastern portion of the LVF. Several source models have already been established with different assumptions regarding the fault geometry or elastic structure (*Wu et al.*, 2006a; *Ching et al.*, 2007; *Hu et al.*, 2007; *Mozziconacci et al.*, 2009; *Cheng et al.*, 2009; *Hsu et al.*, 2009a). We produce our own model to allow for a consistent comparison with interseismic and postseismic slip models.

coseismic slip on the LVF is determined based on the estimate of static displacements derived from the cGPS (33 sites) and accelerometric (38 sites) records (*Wu et al.*, 2006a; *Wu and Wu*, 2007; *Hu et al.*, 2007). The coseismic displacements and the associated uncertainties at the cGPS stations are derived from the least squares fit to the times-series using equation (2.1). The 1-sigma uncertainties are of the order of 1 mm and 4 mm for the horizontal and vertical components respectively. With regard to the coseismic displacements retrieved from the accelerometric records, we initially use the uncertainties estimated by *Wu et al.* (2006a) which are reported to be 2.9 mm for the horizontal components and 1.9 mm for the vertical. Fault slip is determined from a standard least squares inversion of these data, as described in section 2.3. In equation (2.5) λ is chosen to offer the best compromise between smoothness and fit to the data, which lead to $1/\lambda = 0.005$, for more details see Figure S4 in supplement that plots the variation of χ^2 against λ. Uncertainties are renormalized to balance the relative contribution of the accelerometric and GPS data. We imposed the reduced χ^2 to be equal to 1 when computed on each data set separately, *i.e* accelerometric uncertainties must be multiplied by 4.8 whereas uncertainties for inferred coseismic jumps from GPS times series must multiplied by 6.6. These renomalization factors suggest that some sources of errors are not properly taken into account in the initial estimates of the uncertainties (such as those due to heterogeneities of the elastic medium or topography). The renormalized uncertainties seem reasonable (of the order of a few cm)

Our coseismic model (Figure 2.14) is in good agreement with previously published geodetic inversions (*Ching et al.*, 2007; *Hu et al.*, 2007; *Mozziconacci et al.*, 2009; *Cheng et al.*, 2009; *Hsu et al.*, 2009a), but somewhat smoother than the kinematic model of *Mozziconacci et al.* (2009) which incorporates GPS data as well as teleseismic and accelerometric waveforms. According to our model most of the slip occurred on a $10x10\text{km}^2$ patch and peaked to a maximum of 0.91 m at 17 km depth (Figure 2.14). The location of the rupture area is close to what *Mozziconacci et al.* (2009) obtained. Their source is more compact with a peak slip twice as large, probably because of the enhanced resolution afforded by the seismic waveforms (in fact in such a joined inversion the static displacements constrain essentially the final slip distribution while the waveforms provide constrains on the time history of slip). Our model shows no significant slip near the surface (Figure 2.14). This finding is in agreement with field observations and the absence of coseismic offset in the creepmeter record which is located updip of the zone with maximum slip. Few patches display 0.15 to 0.27 m of fault slip, but most of them show a displacement lower than 0.1 m.

The equivalent seismic moment released (M_0) was computed as the sum of the seismic moment of all individual subfaults, assuming a shear modulus (μ) of 30 GPa:

$$M_0 = \mu \sum_i S_i \Delta u_i, \tag{2.7}$$

where S_i is the area of the subfault and Δu_i the computed slip on S_i. Our model estimates the seismic moment to be $1.87.10^{19}$ N.m., in close agreement with the moment of $2.07.10^{19}$ N.m. determined by *Mozziconacci et al.* (2009) assuming a shear modulus of 32 GPa. The equivalent moment Magnitude ($M_w = 6.8$), estimated using *Hanks and Kanamori* (1979) relation :

$$M_w = \frac{2}{3}\left(\log_{10} M_0 - 9.1\right), \tag{2.8}$$

is consistent with the value reported in the Harvard-CMT catalogue.

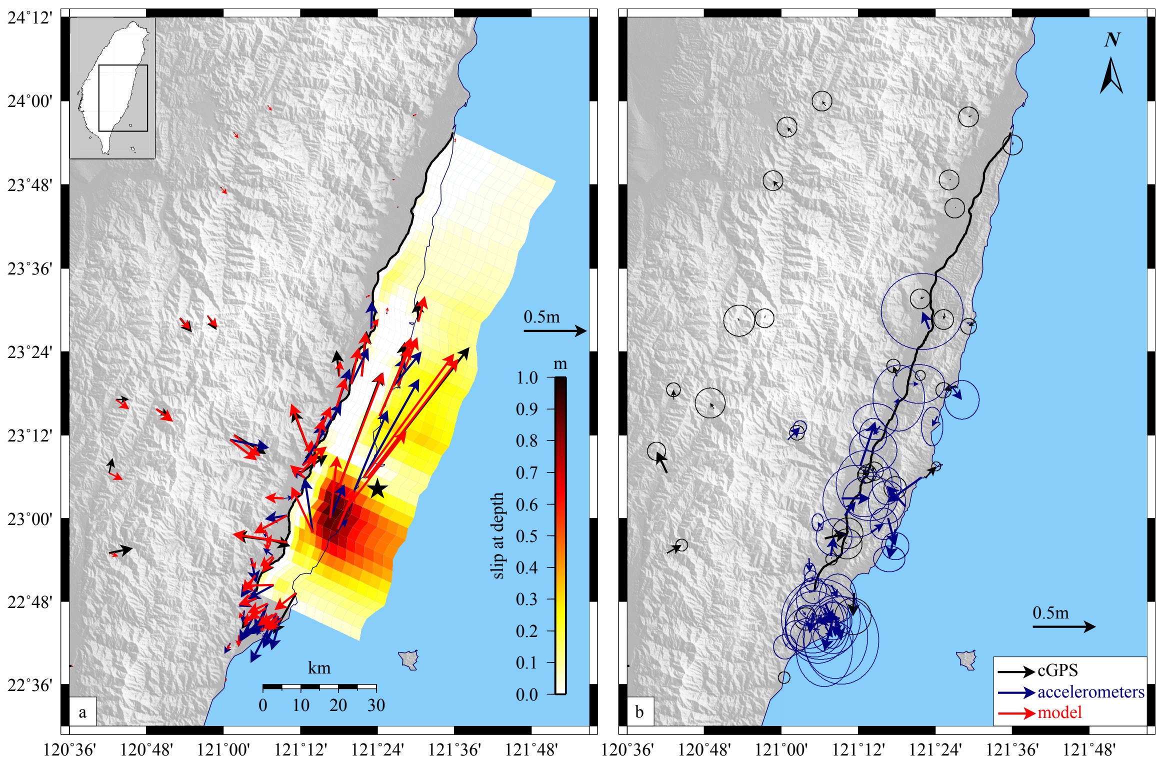

Figure 2.14: Coseismic slip distribution model of the 2003 Mw 6.8 Chengkung Earthquake. (a) The grid shows slip on the fault inferred from the inversion of the static coseismic displacements determined at the CGPS and accelerometric stations, indicated by black and blues arrows respectively. Predictions from our best-fitting coseismic model are plotted in red. (b) Residuals between observed and predicted horizontal displacements. Black star indicates the epicenter of the Chengkung earthquake and black line represents the fault trace of the Longitudinal Valley Fault.

2.6 Pre- and postseismic temporal variation of fault slip rate

2.6.1 Inversion procedure

We now determine the temporal variation of slip at depth before and after the 2003 Chenkung earthquake from modeling the geodetic time series. We use the PCAIM technique (*Kositsky and Avouac*, 2010) since this method has been designed to deal with any kind of time variations of fault slip and allow integrating simultaneously different kind of geodetic measurements and remote sensing data (see also *Lin et al.* (2010); *Perfettini et al.* (2010); *Wiseman et al.* (2011); *Copley et al.* (2012) for examples of applications of that technique). The method is computationally cheap and allows to take advantage of the spatial resolution afforded by the remote sensing data, which are sparse in time but dense in space, with the temporal resolution of the GPS time series which are sparse in space but dense in time.

Times-series are combined to build a data matrix X_0 of dimension $m \times n$ where each row corresponds to the time series of 1 scalar quantity (either shortening measurement from a creepmeter or one component (east, north, up) of a GPS stations), and each column corresponds to a given epoch of data acquisition (all data acquired at a given are listed under the same column). Therefore X_{ij} represents the displacement at station i at the j^{th} step in time. Infinite uncertainties is assigned to missing data measurement. The data matrix is then centered (equation 2.9) before applying a Singular Value Decomposition (SVD):

$$X(i,j) = X_0(i,j) = \mu \sum_i S_i \Delta u_i, \tag{2.9}$$

$$X = U.S.V^t, \tag{2.10}$$

where the column vectors of U are the eigenvectors of the spatial covariance matrix XX^t, the column vectors of V are the eigenvectors of the temporal covariance matrix X^tX, and S is the rectangular diagonal matrix with elements equal to the eigenvalues of X, ordered decreasingly (*Kositsky and Avouac*, 2010). The components are determined from a weighted least squares procedure that takes into account data uncertainties. The principle of PCAIM is to combine Principal component analysis (PCA) (equation 2.10) with the inversion for slip at depth based on the theory of dislocation in an elastic half space (equation 2.2). Therefore, each column vectors of U are inverted to get the corresponding principal slip distribution l defined by:

$$U = G.l. \tag{2.11}$$

This equation is solved from the standard least-squares procedure with Laplacian regularization described in section 2.3. The fault slip history is retrieved by linear composition:

$$X = (G.l)\,.S.V^t = G.\left(l.S.V^t\right), \tag{2.12}$$

where $(l.S.V^t)$ is the slip on each patches of the fault over time. Only statistically relevant Principal Components (PCs) of the decomposition should be kept. The number of useful components is assessed from computing the fraction of variance of the data matrix accounted by the k^{ith} component which is simply:

$$\frac{\lambda_k^2}{\sum_{i=1}^{r}\lambda_i^2}, \tag{2.13}$$

where r is the rank of the diagonal matrix S (number of non zero eigenvalues). One can also consider the variation of the χ^2 as a function of the number of principal components used and determine the number of useful components using a f-test (*Kositsky and Avouac*, 2010).

A dataset very sparse in time, such as the PS-ALOS data or the campaign GPS data, cannot be incorporated in the PCA decomposition but can be used to place constraints on the inversion of the principal components. The set of linear equation (2.12), considering only the meaningful components, is then inverted jointly with the condition that the slip distribution, at the appropriate epochs, predict the sparse dataset. Consequently these data bring constraints on the spatial distribution of the principal slip distribution represented by the vectors l but not on the time functions V. As in section 2.5, we balance the weight put on each data used in PCAIM by rescaling the uncertainties so that the weighted rms of the residuals (or χ^2_{red}, equation 2.4), computed for each dataset separately, is equal to 1. Weighting is adjusted iteratively, generally only 1 or 2 iterations are necessary. Assessing the appropriate weighting to assign to a sparse dataset, relative to the weight placed on fitting the U vectors is not straightforward. For example, in the case of a dataset consisting of cGPS and SAR data the GPS time series should bring a stronger constrain since they provide a daily, uncorrelated record of absolute position. However, through the PCAIM procedure, we reduce drastically the number of input parameters by a applying an SVD. Therefore ALOS dataset becomes over-predominant whereas there is an inherent redundancy in the information provides by PS, directly correlated with the StaMPS procedure itself. As the data covariance is not an output of the StaMPS processing, to circumvent that issue, we arbitrarily penalize the ALOS dataset by increasing estimated errors 10 times (Table 2.6.2). Others data uncertainties have been renormalized to get a χ^2_{red} of 1.

We carry on separate inversions for the periods preceding and following the earthquake. The two inversions are thus independent and any similarity between these solutions has to come from the data rather from the decomposition.

2.6.2 Postseismic inversion

We model the time-evolution of fault slip on the LVF over 7 years following the Chengkung earthquake using all the geodetic data and InSAR data available over that period. A PCA decomposition is applied to the cGPS and creepmeters stations time series. Based on variation of the misfit as a function of the number of principal components we determine that the first four components are significant (Figure 2.15 and Figure S5 in supplements). These four components capture well the spatio temporal variation of postseismic relaxation and the seasonal variations of surface displacement. The weight put on Laplacian smoothing and renormalization factors are listed in Table 2.6.2 along with the rms values obtained from our inversion

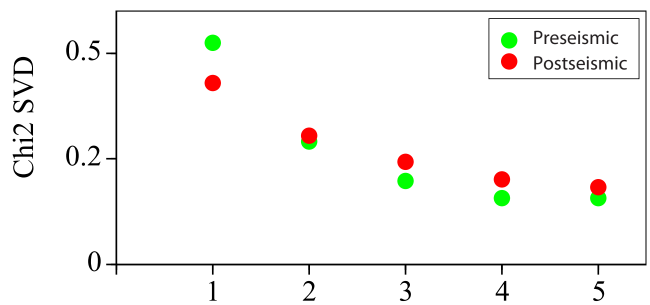

Figure 2.15: Misfit between times series (GPS and creepmeter stations) and reconstructed displacements from the PCA decomposition as the number of principal components increases. Misfit is quantified from reduced chi-square as defined in equation 2.5.

	Secular		Coseismic		Postseismic		Preseismic	
$1/\lambda$	0.1		0.005		0.04		0.06	
	f	rms	f	rms	f	rms	f	rms
ALOS	5	3.8 (mm/yr)			10	3.0 (mm/yr)		
cGPS	60	4.9 (mm/yr)	6.6	6.7 (mm)	0.3	6.5 (mm)	0.3	10.3 (mm)
creepmeter	60	0.5 (mm/yr)			0.3	2.2 (mm)	0.2	1.8 (mm)
campaign GPS	40	2.6 (mm/yr)					8.9	9.0 (mm/yr)
leveling	0.2	2.6 (mm/yr)			3.9	3.3 (mm/yr)		
accelerometers			4.8	8.3 (mm)				

Table 2.3: root mean square (rms) and normalization factors (f).

Figure 2.16 shows the slip distribution model over this time period. Temporal variation of slip at depth is discussed in more details in section (2.7). The fit to the cumulative displacements measured at the cGPS stations is presented in Figure 2.17, and the fit to the InSAR and leveling data is presented in supplementary Figures (S7 and S8). Time variations of surface displacements predicted by the model are plotted in Figure 2.4 for cGPS and the creepemeter time series at a few sites surrounding the coseismic area. Others times-series predictions can be found in supplementary materials (Figures S1, S2 and S3). The principal slip distribution l and their associated time

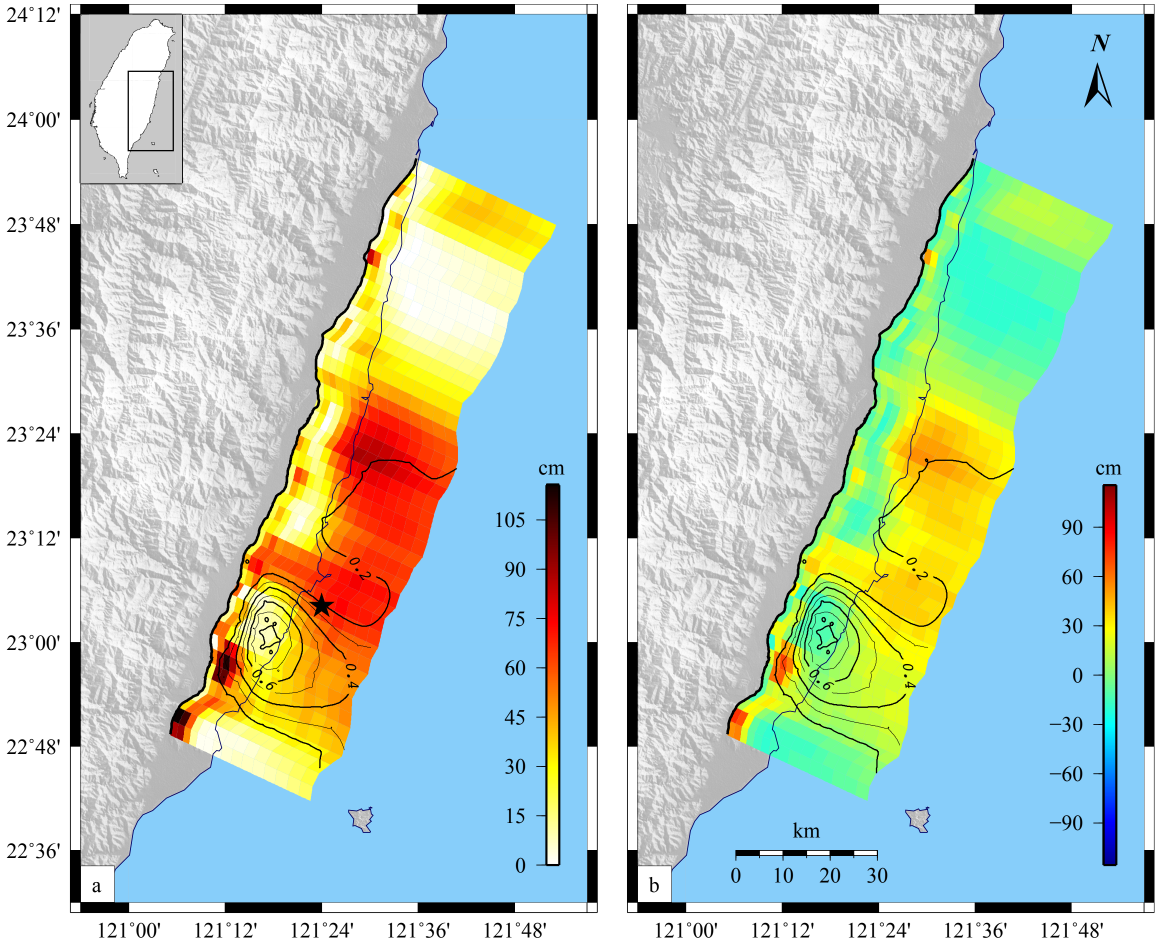

Figure 2.16: Postseismic slip distribution model following the Mw 6.8, Chengkung earthquake of 2003. (a) Cumulative slip on the LVF over the period between 12/11/2003 and 11/26/2010, determined from PCAIM inversion of CGPS and creepmeters time series, leveling data (from 9/1/2007 to 31/20/2010) and PS ALOS cumulative displacement between 1/29/2007 and 6/2/2010. Black star indicates the epicenter of the 2003 Chengkung earthquake. Back curves show contour lines of coseismic slip distribution model of the Chengkung earthquake (Figure 2.14). (b) Difference between postseismic slip and secular slip predicted from the secular model of (Figure 2.10).

functions V are shown in supplementary Figure S6 and S5.

The spatial pattern of aseismic creep in the postseismic period (Figure 2.16a) turns out to be very similar to the secular pattern (Figure 2.10a) with enhanced slip of up to 72 cm around the coseismic rupture (Figure 2.16b). According to this model (Figure 2.16b), afterslip over the 7 years following the Chengkung earthquake have released the cumulative moment of $1.53.10^{19}$ N.m, about 0.8 times the coseismic moment.

2.6.3 Preseismic slip model

We also used the PCAIM procedure to analyze the temporal variation of fault creep before the 2003 earthquake, between January 1997 and December 2003. The spatial resolution is much worse than

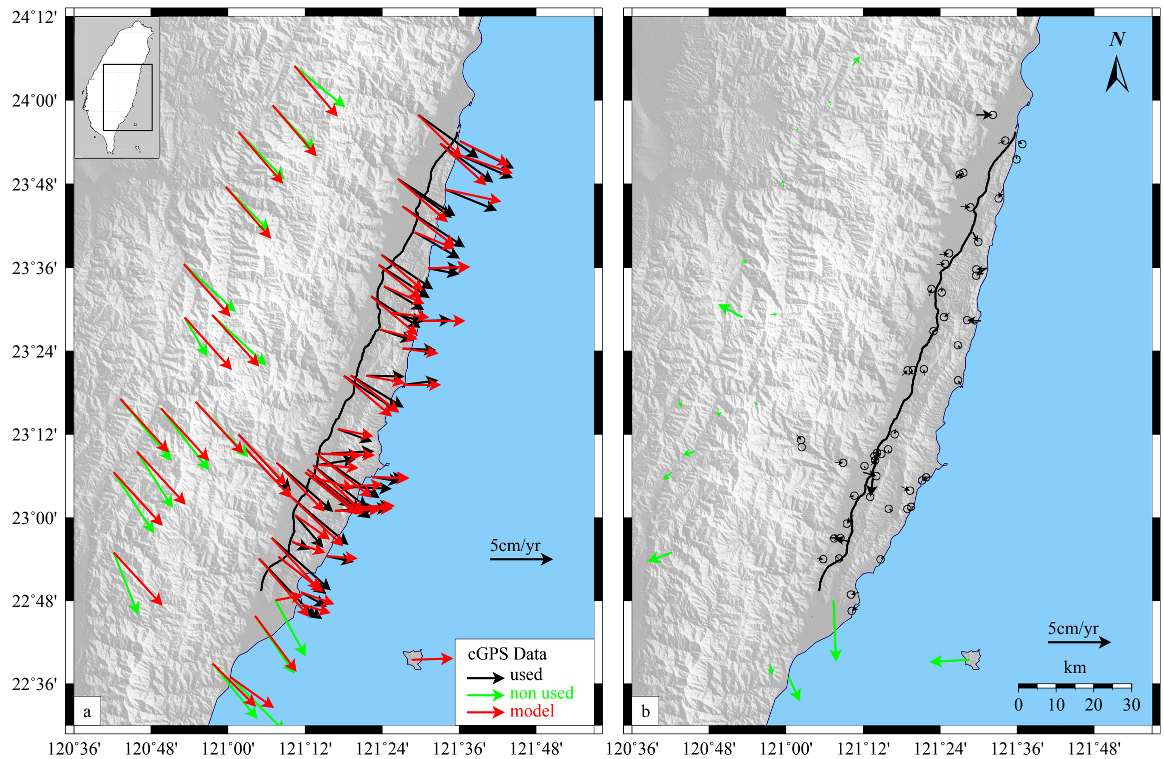

Figure 2.17: Postseismic slip distribution model, fit to geodetic data. (a) Comparison between observed and predicted horizontal displacement over the time period from 12/11/2003 to 11/26/2010. The reference frame is Philippine Sea Plate fixed. The cGPS data which were used or not in the inversion are plotted respectively as black and green arrows. Corresponding predictions of the postseismic slip model of 2.16 are displayeds in red. (b) Residuals from the inversion with corresponding error ellipses. Same color coding as in (a).

in the postseismic period since only 20 continuous GPS stations are available for this time period and among them, only 4 stations have records before 2002. To improve the resolution power of the inversion, we augment the dataset with the campaign GPS measurements which were acquired between 1992 and 1999. These data are treated as sparse in the PCAIM inversion. Creepmeter time series have also been incorporated in this inversion since we have strain measurements across the fault back to 1998.

Variation of the total χ^2 in function of the number of principal components show that 3 components only are significant (*i.e.*, needed to reconstruct the original time series within uncertainties). Most of the signal is explained by the first component (Figure 2.15) which is linear in time (Figure S9 in supplements). The weight put on Laplacian smoothing and renormalization factors are listed in Table 2.6.2 along with the rms values obtained from our inversion. The principal slip distributions l and their associated time functions V are shown in supplementary Figures S10 and S9.

The distribution of slip rate averaged over the preseismic period is plotted in Figure 2.18. Fit to the mean surface velocities at the continuous GPS stations and GPS campaign sites is displayed in Figure 2.19. Time variations of surface displacements predicted by the model are plotted in Figure 2.4 at few continuous GPS stations and for the creepemeter. Comparison of observed and predicted times-series at other stations can be found in supplementary materials (Figures S1, S2 and S3).

As Figure 2.18(b) emphasizes, the interseismic model derived from the PCAIM procedure and the secular slip rate model are very similar. Differences between the two models is most likely related to the lower resolution of the time-dependent interseismic inversion. This modeling indicates that aseismic slip over the 7 years preceding the Chengkung earthquake has been essentially steady-state and released a cumulative moment of $3.86.10^{19}$ N.m, which is about 2 times the coseismic moment which was released during the Chengkung earthquake.

2.7 Slip history on the LVF in the Chengkung earthquake area over the 1997-2011 period

Based on the results presented above it is now possible to describe the time evolution of slip on the LVF over the study period. Here we focus on the Chengkung earthquake area where the temporal variations are the most noticeable. Also, contrary to the Northern portion of the Longitudinal Valley fault, this area is probably not influenced by the Ryukyu subduction zone. The rest of the fault is not showing any significant temporal variation.

Figure 2.20 provides a synthetic view of the time evolution of slip in the Chengkung earthquake area. The map view shows a close-up view of the distribution of interseismic creep rates which was derived from the inversion of the secular surface strain rate (Figure 2.10a). We also show the time

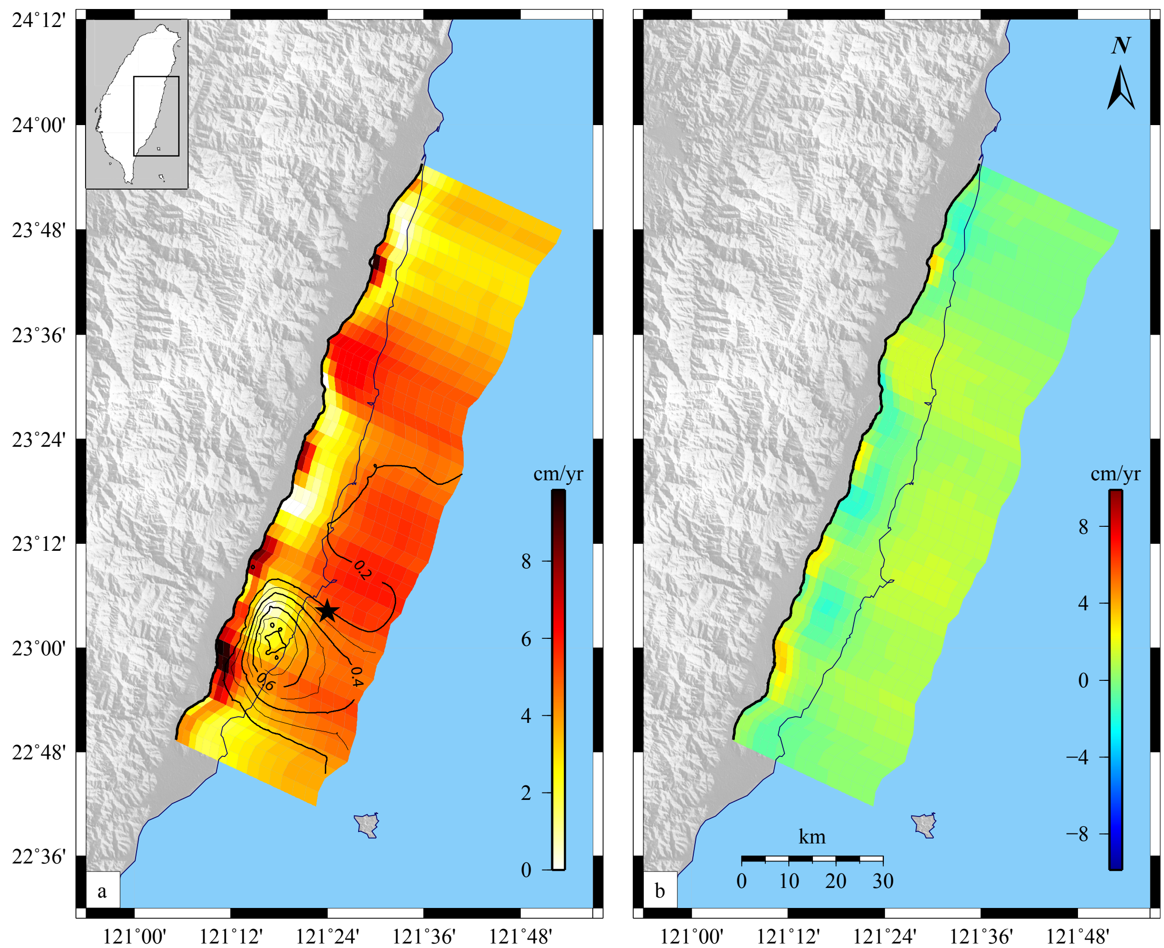

Figure 2.18: Preseismic slip distribution model. (a) Mean slip rate on the fault over the 1/1/1997 to 12/12/2003 period, inferred from PCAIM inversion of the campaign GPS data, the CGPS and creepmeter time series. Black star indicates the epicenter of the 2003 Chengkung earthquake. Back curves are contour lines of the coseismic slip distribution model for the 2003 Mw 6.8 Chengkung Earthquake (Figure 2.14). (b) Difference between preseismic slip rate and secular slip rate predicted from the secular model of (Figure 2.10).

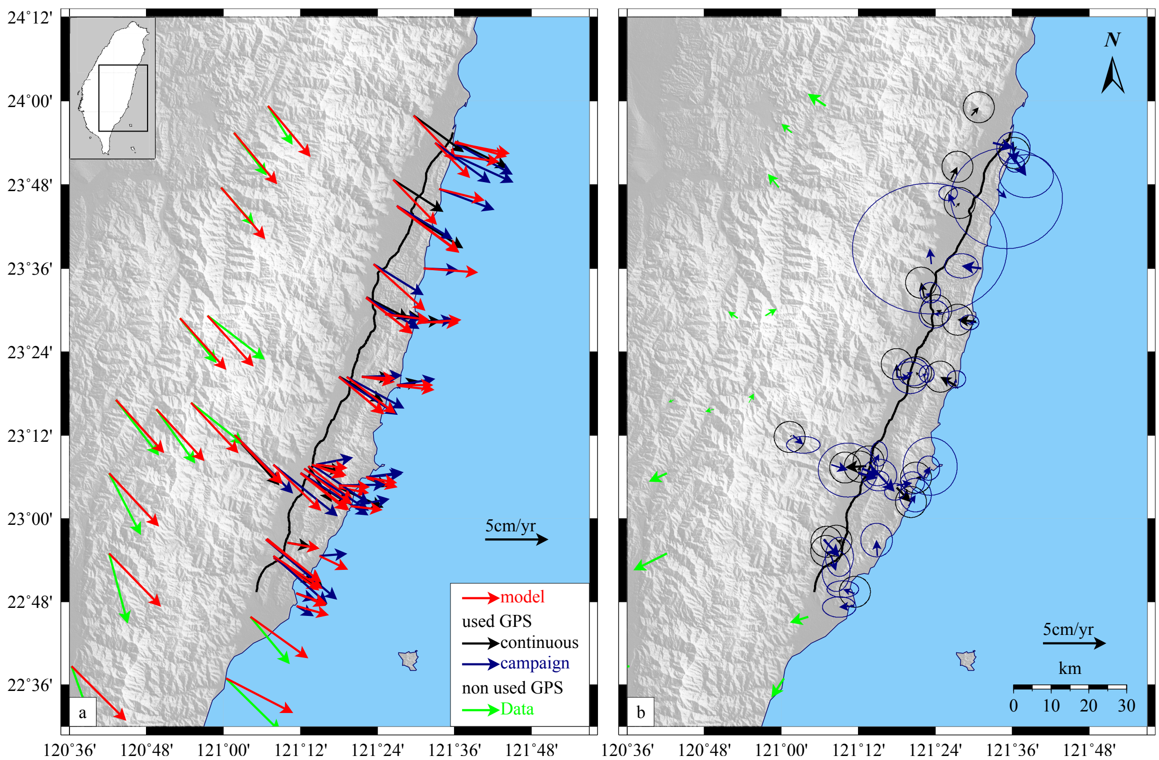

Figure 2.19: Preseismic slip distribution model, fit to geodetic data. (a) Comparison between observed and predicted horizontal velocities, averaged over the time period (from 1/1/1997 to 12/12/2003). The reference frame is Philippine Sea Plate fixed. The GPS data used in this inversion are plotted respectively as dark blue and black arrows for the campaign and continuous GPS measurements. Green arrows stand for the GPS stations that were not used in the inversion but which are plotted for reference. Corresponding predictions of the interseimic coupling model are displays in red. (b) Residuals from the inversion with corresponding error ellipses. Same color coding as in (a).

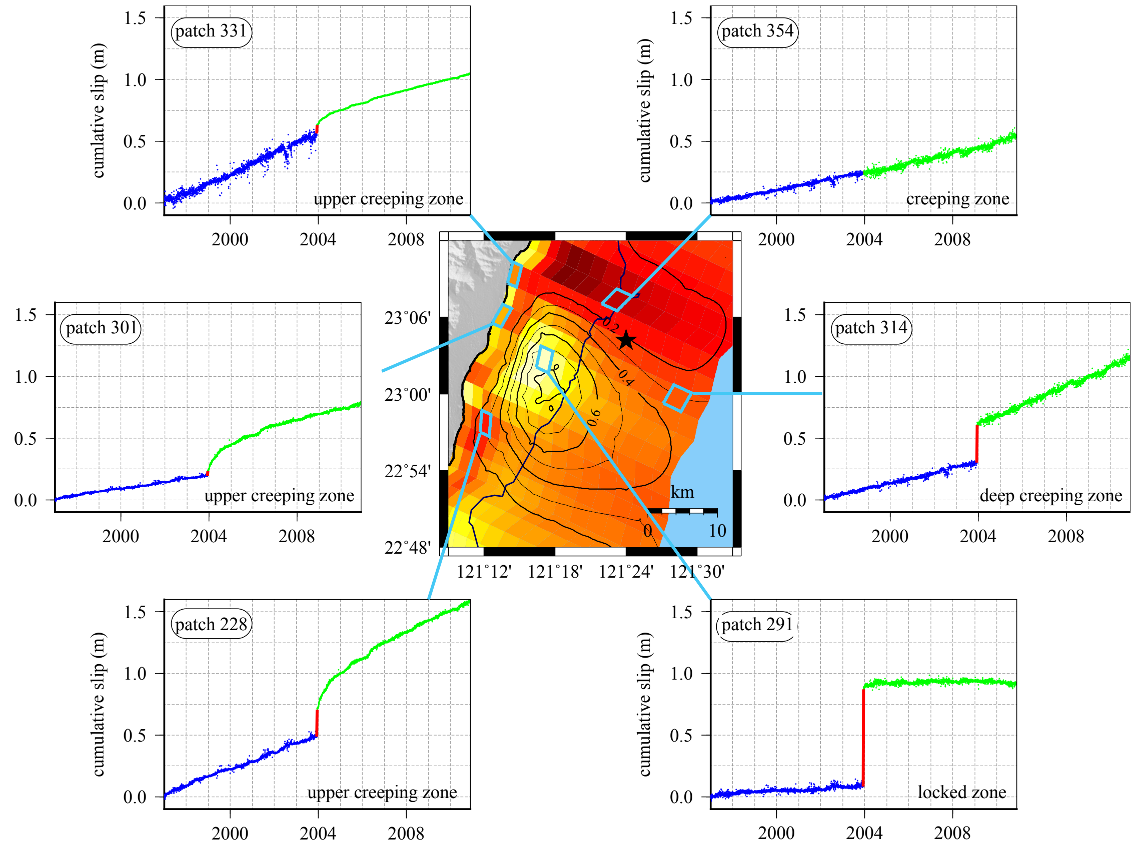

Figure 2.20: Slip at depth through time obtained from combining PCAIM inversions of pre- and post-seismic period and coseismic slip due to the Chengkung earthquake. Map view shows a close-up view of the secular slip rate distribution over the whole study period (see Figure 2.10a for location), with contour lines of the coseismic slip model (black lines) and epicenter (star) of the 2003 Chengkung earthquake. Graphs around the map view show the time evolution of slip at 6 patches along the direction of the slip vector predicted by the block motion of the Coastal Range relative to the Central Range. Patch 331, 301, and 228 sample the upper creeping zone. Patch 291 is characteristic of the zone which was locked before the Chengkung earthquake, slipped during the event and relocked immediately after. Patches 314 and 354 illustrate the behavior of deeper fault portion which is most poorly resolved.

evolution of slip at a number of representative patches, retrieved from combining the source model of the earthquake with the PCAIM models for pre- and post-seismic periods. The cumulative slip vector at each epoch is projected on the direction of the long term slip vector predicted by the block motion of the Coastal Range relative to the Central Range. Our model indicates that over the 14 years between 1997 and 2011 this fault area has slipped by a total of 1 m to 1.5 m. This is approximately the cumulative slip for that period of time expected from the long term oblique convergence between the Coastal Range and the Central Range. The results show that slip resulted from a combination of steady creep, unsteady creep and seismic slip in proportions that vary in space.

Comparison of the secular pattern of creep rate with the slip contour lines of the coseismic rupture during the Chengkung earthquake clearly shows that the rupture extent coincides closely with an area that has remained mostly locked in the interseismic period and relocked immediately after. Time evolution of slip for patch 291 is instructive in that regard (Figure 2.20). This patch lies at depth of about 15 km in the middle of the zone with peak seismic slip. According to our model, this patch slipped by about 0.8 m and relocked immediately after the earthquake. The earthquake nucleated at the edge of this locked zone (see epicenter in Figure 2.20), ruptured this entire patch and did not propagate much into the surrounding creeping areas, except at depth where the overlap could be partially due to the smoothing induced by the regularization of our inversions, as Figure 2.7 illustrates. The rupture failed in particular to propagate across the shallow portion of the fault at depth less than about 7 km (see slip history at patch 301 in Figure 2.20) in agreement with the absence of surface ruptures observed in the field (*Lee et al.*, 2006) and the other source models of this earthquake (*Wu et al.*, 2006a; *Hu et al.*, 2007; *Wu and Wu*, 2007; *Mozziconacci et al.*, 2009).

The secular slip rate on the upper part of the fault, which is creeping in the interseismic period as the InSAR and creepmeter measurements indicate, varies along strike (Figure 2.20). Patches 331 and 228 show similar behavior for the interseismic period: high creep rate was inferred (8.2 cm/yr for 331 and 6.7 cm/yr for 228) whereas patch 301 displays smaller creep velocity (2.9 cm/yr), likely because it is in the stress shadow of the locked segment (see for example *Hetland and Simons* (2010) for a modeling study illustrating this effect). During coseismic patches 331 and 301, which corresponds to the uppermost part of the fault, record only few centimeters of slip. On the contrary, patch 228, which stands at 9 km depth, recorded a coseismic jump of $\sim$ 20 cm. The creep rate increased abruptly right after the earthquake and then relaxed, leading to an approximately logarithmic increase of slip with time, but at different rate for the 3 patches. The maximum displacement is recorded at patch 228, where the slip rate after 7 years is 1.2 times higher than before December 2003. Patch 301 also slip at faster rate (4.8 cm/year, *i.e* 1.6 times faster), but patch 331 on the contrary undergoes a decrease in slip velocity after the Chengkung earthquake (4.8 cm/yr).

Evidence for transient afterslip at depth below the rupture is less clear due to the poor resolution of the inversions. No transient is seen at patch 354, which seems to have been creeping at a nearly constant rate (3.3cm/yr) throughout the study period. Patch 314 which, according to our model has been creeping in the preseismic period at 4.8 cm/yr, slipped during the Chengkung earthquake (0.3 m) and creeps more rapidly in the post-seismic period (6.7 cm/year) but we do not observe the typical logarithmic behavior seen at shallower depth, suggesting a possible way longer relaxation time. Nevertheless it is hard to tell if this observation is really required by the data and warrants interpretation.

2.8 Discussion

2.8.1 Spatial distribution of seismic and aseismic creep, role of the Lichi Mélange

The dataset assembled in this study demonstrates that most of the southern portion of the LVF is creeping at the surface, though at a rate lower than the long term slip rate required by the block motion of the Coastal Range with respect to the Central Range. By contrast, no surface creep is detected along the northern half of the LVF, which displays a high stress-build up (Figure 2.10b).

Comparison with surface geology support earlier inferences (e.g., *Hsu et al.*, 2009a) than the Lichi Mélange would be responsible for promoting aseismic creep. This clay-rich formation, interpreted as a collision mĺange (*Chang et al.*, 2000, 2001, 2009; *Huang et al.*, 2006b, 2008), crops out in the Coastal Range and seems to fringe the creeping segment of LVF (Figure 2.2a). This formation does not extent along the northern segment of the LVF, where only isolated outcrops have been interpreted to correspond to that particular formation (*Teng*, 1980a). It is noteworthy that the seismic crisis of 1951, with its 4 $M_w > 6.8$ shocks, did produce surface ruptures only along the northern portion of the LVF (*Shyu et al.*, 2007; *Lee et al.*, 2008). The southern segment of the fault can nevertheless also produces large seismic event as the Chenkung earthquake demonstrates. However the rupture occurred in the 10-20km depth range and didnt reach the surface. Our interseismic model indicates that the earthquake actually ruptured a fault patch that was locked before 2003 and relocked immediately after and is surrounded by a zone that is dominantly creeping. The Lichi mĺange is an important factor controlling along strike variations of creep rate but whether it is through the intrinsic properties of its dominant minerals or whether it is related to the hydrological properties of this formation is unclear at this point.

2.8.2 Seismic and aseismic slip budget, implication for the return period of $M_w > 6.8$ earthquakes on the LVF

Our modeling results allow estimating the relative proportion of seismic and aseismic slip on the LVF and draw inferences regarding the return period of large earthquakes in this area. The reader should be aware of the large uncertainties involved in this discussion. It is particularly difficult to formally take into account all the possible sources of errors due not only to the measurements uncertainties but also to the modeling assumptions. For example, it is probably not correct to assume that the CeR and CoR blocks can be consider rigid in the long run nor to neglect the strain associated with the complicated junction with the Ryuku subduction zone north of the Longitudinal Valley. However it is still worth illustrating the kind of questions which can be addressed based on the modeling attempt presented in this study.

Interseismic strain implies a rate of accumulation of slip-potency ($SP_{deficit}$), or equivalently, moment deficit which can be computed from integrating the slip-rate deficit over the locked fault zones (section 2.4.3 and 2.4.2):

$$M_{0_{deficit}} = \mu.SP_{deficit} = \mu \sum_i V_i.ISC_i.S_i, \tag{2.14}$$

where S_i is the area of the subfault, V_i is the long-term slip rate inferred in section 2.4.2 based on the CeR/CoR pole and the interseismic coupling coefficient ISC_i quantifies the degree of locking defined in section 2.4.3. We estimated the moment deficit rate to be $2.77.10^{18} N.m.yr^{-1}$ for the whole LVF. If we consider the southern section only, with the upper boundary defined as the transition between the creeping section and the locked zone in the north (Figure 2.10b), we obtain a value of $1.12.10^{18} N.m.yr^{-1}$ (Table 2.8.2). Then given the cumulative moment released by the coseismic slip and the following afterslip (Table 2.8.2) inferred in this study, the return period of earthquake similar the Chengkung earthquake can be estimated from the equation:

$$T = \frac{M_{0_{coseismic}} + M_{0_{postseismic}}}{M_{0_{deficit}}}. \tag{2.15}$$

Based on this equation, we get a return period of $\sim$ 13 years if we considered the whole LVF, and $\sim$ 34 years for the southern section. These estimate seems reasonable given that 5 earthquakes with $M_w \geq 6.8$ occurred over the last century (*Shyu et al.*, 2007; *Chung et al.*, 2008; *Lee et al.*, 2008; *Wu et al.*, 2008a). Therefore, this analysis shows there is no need for larger or more frequent earthquakes than those known historically to balance the deficit of slip due to the pattern of locking on the LVF in the interseismic period.

	Models	Moment	equivalent M_w
ISC (deficit)$_a$	all LVF	$3.31.10^{18}$ N.m.yr^{-1}	6.28
	south LVF	$1.35.10^{18}$ N.m.yr^{-1}	6.02
Preseismic$_a$	all LVF	$7.69.10^{18}$	6.52
	south LVF	$5.20.10^{18}$	6.41
Coseismic	all LVF	$2.50.10^{19}$ N.m	6.86
	south LVF	$2.26.10^{19}$ N.m	6.83
Postseismic$_b$	all LVF	$1.92.10^{19}$ N.m	6.79
	south LVF	$2.34.10^{19}$ N.m	6.85

Table 2.4: Moments and moment Magnitudes inferred from inversion models. (a) Moments and moment Magnitudes values are cumulated over one year. (b) cumulative value after $\sim$ 7 years, for the afterslip only, *i.e* minus the secular model.

It is then instructive to compare our estimate of the return period of a $M_w > 6.8$ earthquakes on the LVF with the frequency-magnitude distribution of instrumental earthquakes in the area, displayed in Figure 2.21. For that purpose we used the 1991-2010 seismicity catalog from *Wu et al.*

(2008b), selecting events laying on the southern half portion of the LVF, where our model is best constrained (see seismicity map in Figure S12). Seismic data follows the Gutenberg-Richter law:

$$\log_{10}(N(m > M_w)) = a - bM_w, \tag{2.16}$$

where N is the number of events which have a moment magnitude greater or equal to M_w; a and b are constants with a typical value of 1 for the b parameter in seismically active regions. We divided the dataset in three time periods: from 1/1/1991 to 12/31/2009 (all catalog), from 1/1/1991 to December 9^{th} 2003 (before 2003 Chenkung Earthquake) and from December 10^{th} 2003 and thereafter. Above their magnitude of completeness (which is about 1.8) those three subsets of the main catalog return a similar b value of 0.95 for the complete dataset to 0.94 and 0.89 for seismicity selected before and after the main shock respectively (Figure 2.21). The return period of Chengkung-type earthquake inferred from this study can be plotted in this diagram (Figure 2.21). It shows a nice consistency with the instrumental catalog since the Gutenberg-Richter distribution defined above yields a return period of $\sim$ 24 years for $M_w = 6.8$ earthquake if we were considering the whole LVF and $\sim$ 36 years if we only selects earthquakes in the southern section of the LVF (Figure 2.21).

We can also estimate the fraction of slip potency (or equivalently release moment) which results from aseismic (α), or seismic (γ) over the long term average, assuming that known seismicity is representative of the long term behavior. The fraction of aseismic slip is

$$\alpha = \frac{T.\sum_i V_i.(1 - ISC_i).S_i + M0_{postseismic}/\mu}{T.\sum_i V_i.S_i}. \tag{2.17}$$

This calculation tends to provide an overestimate as it assumes that all of the measured geodetic strain results from aseismic creep, except for the effect of the Chengkung earthquake. We estimated this fraction to about 77% for the whole LVF. If we focus on the southern portion where the model is more reliable (not biased by interseismic strain associated with the Ryuku subduction zone), we get an even larger value of 92%. This estimate is probably representative of the long term average as the study period is long enough compared to the return period of large earthquakes so that the average interseismic creep pattern is reasonably well constrained, and the contribution of transient aseismic creep due to afterslip following the Chenkgung earthquake is only a small fraction of the total budget. This estimate has a large uncertainty, in relation with uncertainties on our slip models among other factors. The fraction of seismic slip is :

$$\gamma = \frac{\sum M_{0_i}}{\mu.t_{cat}.\sum_i V_i.S_i}, \tag{2.18}$$

where the numerator accounts for the moment released by all earthquakes on the LVF during the study period t_{cat}. This quantity can be bracketed if we consider on one end only the Chengkung

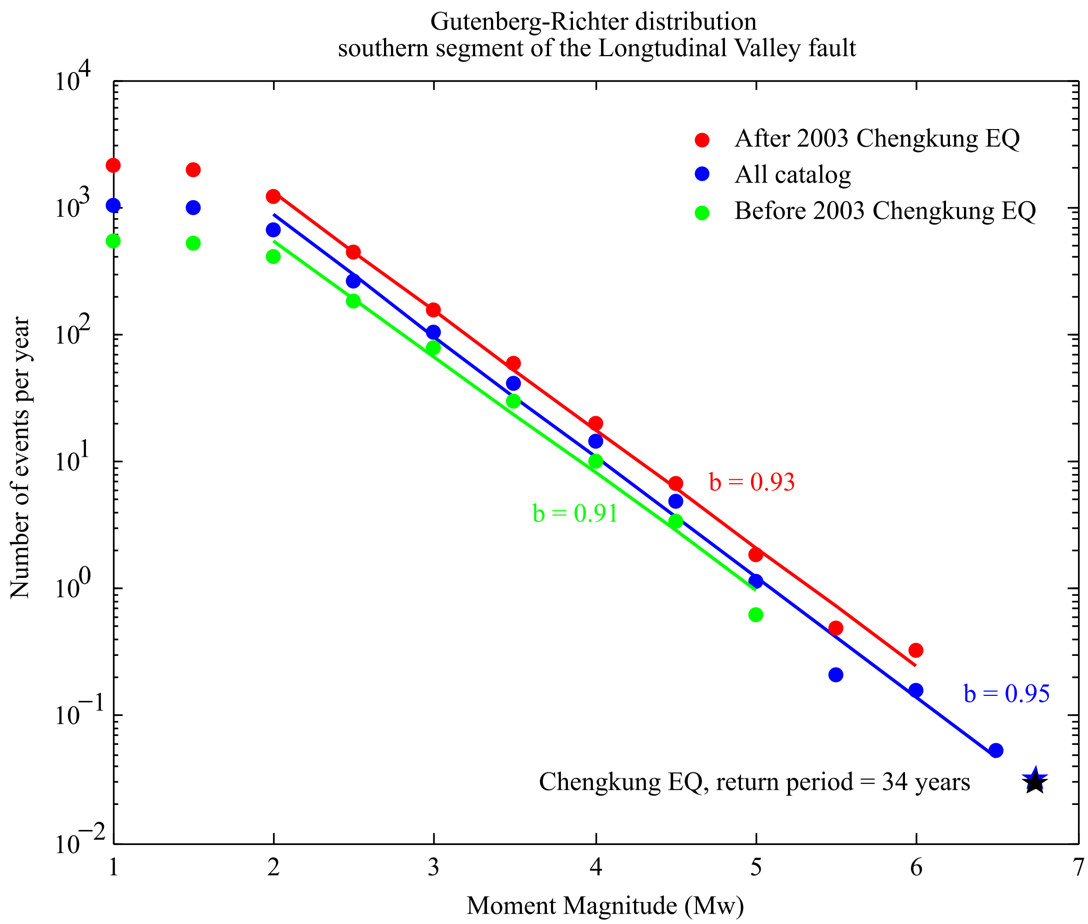

Figure 2.21: Frequency-magnitude distribution of seismicity from 1991 to 2010 on the Longitudinal Valley, using the catalog from *Wu et al.* (2008b), for the southern portion of the fault (see S12a in supplements for location). The graph shows, in ordinate, the number of events with moment magnitude equal or larger than a given value reported in abscissa. We divided the catalog in three time periods: in blue from 1991 to 2010 (all catalog), in green from 1991 to December 9^{th} 2003 (before 2003 Chenkung Earthquake) and in red from December 10^{th} 2003 and thereafter. Lines are Gutenberg-Richter distribution computed for magnitude $M_w \geq 2$. Returned b value are respectively 0.95 for the all catalog, 0.92 before the Chengkung earthquake and 0.95 for seismicity selected after the main shock. Black star shows the return period computed from this study for Chengkung-type earthquake ($M_w = 6.8$) from balancing the seismic and aseismic slip budget on the LVF. .

earthquake, which unambiguously occurred on the LVF, and on the other end assume that all the earthquakes which recorded in the study area over the study period occurred on the LVF and add their scalar seismic moments by extrapolating the number of earthquakes with magnitude below the detection threshold based on the Gutenberg-Richter law (Figure 2.21). We thus estimate the numerator to between $1.87.10^{19}$ and $2.77.10^{19}$ for the all fault, and between $1.68.10^{19}$ and $2.40.10^{19}$ for the southern segment. The fraction of seismic slip is then estimated to between 14% and 21% if all the LVF is considered. It is estimated to between 20% and 28% considering only the southern section where most of the aftershocks occur (see supplement S12). This estimate is not necessarily representative of the long term average given that the earthquake catalog does not cover several earthquake cycles so that the moment released by the largest earthquakes on the LVF in the long run is poorly constrained. Despite all the uncertainties in those estimate it is interesting to note that the slip budget approximately closes up.

2.9 Conclusion

This study demonstrates that a large fraction of the long term slip budget on the Longitudinal Valley Fault (LVF) in the 0-26km seismogenic depth range (as defined by local seismicity) is actually the result of aseismic creep. We estimate that fraction to about 80-90%. The spatial pattern of aseismic creep on the LVF is very heterogeneous, showing both along dip and along strike variations. Creep is observed at the surface along the southern portion of the LVF where it seems to correlate with Lichi Mélange. The Mw 6.8 Chenkgung earthquake of 2003 ruptured entirely a 12.5 km x 15.8 km patch that had remained locked in the interseismic period which extends at depth between 8 and 20 km. The earthquake seems to have nucleated at the boundary of the locked zone, where stress must build up fast in the interseismic period. Then it propagated through the locked patch but fail to propagate much into the surrounding creeping areas Figures 2.10, 2.14 & 2.18). Afterslip, due to enhanced creep in the immediate vicinity of the rupture, released a moment equivalent to 0.8 time the seismic moment of the earthquake and increased approximately logarithmically with time. This time evolution is consistent with the time evolution of afterslip excepted from velocity-strengthening friction (*Marone et al.*, 1991; *Perfettini and Avouac*, 2004). These observations suggest that the location and the extent of seismic asperities are largely controlled by permanent rheological properties of the fault zone, which, in the present case, seems to relate to the lithology.

To first order, this simple picture compares well with theoretical models of seismic cycle based of lateral and depth variation of frictional properties of faults (e.g. *Lapusta et al.*, 2000; *Rice and Ben-Zion*, 1996; *Scholz*, 1998). In those models, aseismic slip occurs in velocity strengthening areas during the interseismic period until instability occurs at the boundary between velocity strengthening and velocity-weakening zones, leading to the nucleation of seismic events that ruptures previously locked velocity weakening zones. Depending on the size and on the frictional properties of the velocity strengthening zones, seismic events are able to propagate through the creeping sections or are stopped by them (*Kaneko et al.*, 2010). Then, relaxation of coseismic stress results in acceleration of aseismic slip in the velocity strengthening areas until it comes back to interseismic rates. Our study thus confirms the suggestion that aseismic patches tend to play a key role in arresting seismic ruptures, presumably because aseismic creep prevent stress build up and because of the presumably rate-strengthening rheology absorbs energy during seismic rupture propagation (*Kaneko et al.*, 2010). We see no clear evidence that Thermal Pressurization could have facilitated propagation of the rupture into the creeping segment as could happen according to numerical simulation (*Noda and Lapusta*, 2010, 2013). The LVF thus stands out as a candidate example where a dynamic model of the seismic cycle could be designed and calibrated from comparison with geodetic and seismic data as has been done on the Parkfield segment of the San Andreas Fault (*Barbot et al.*, 2012).

Seismic and aseismic slip on LVF - Supplementary material

July 23, 2013

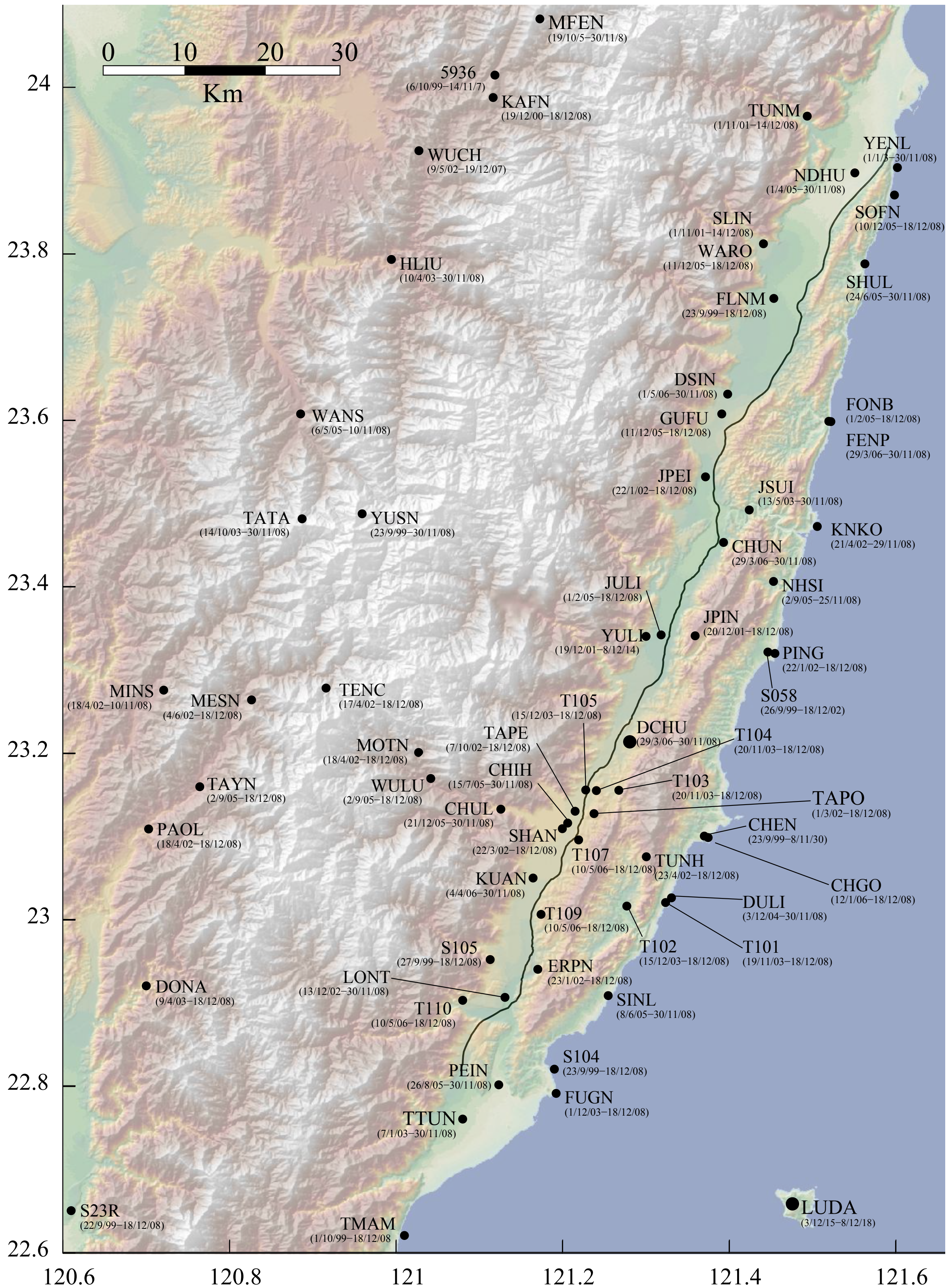

Figure S1: Locations of continuous GPS stations with the corresponding date of records.

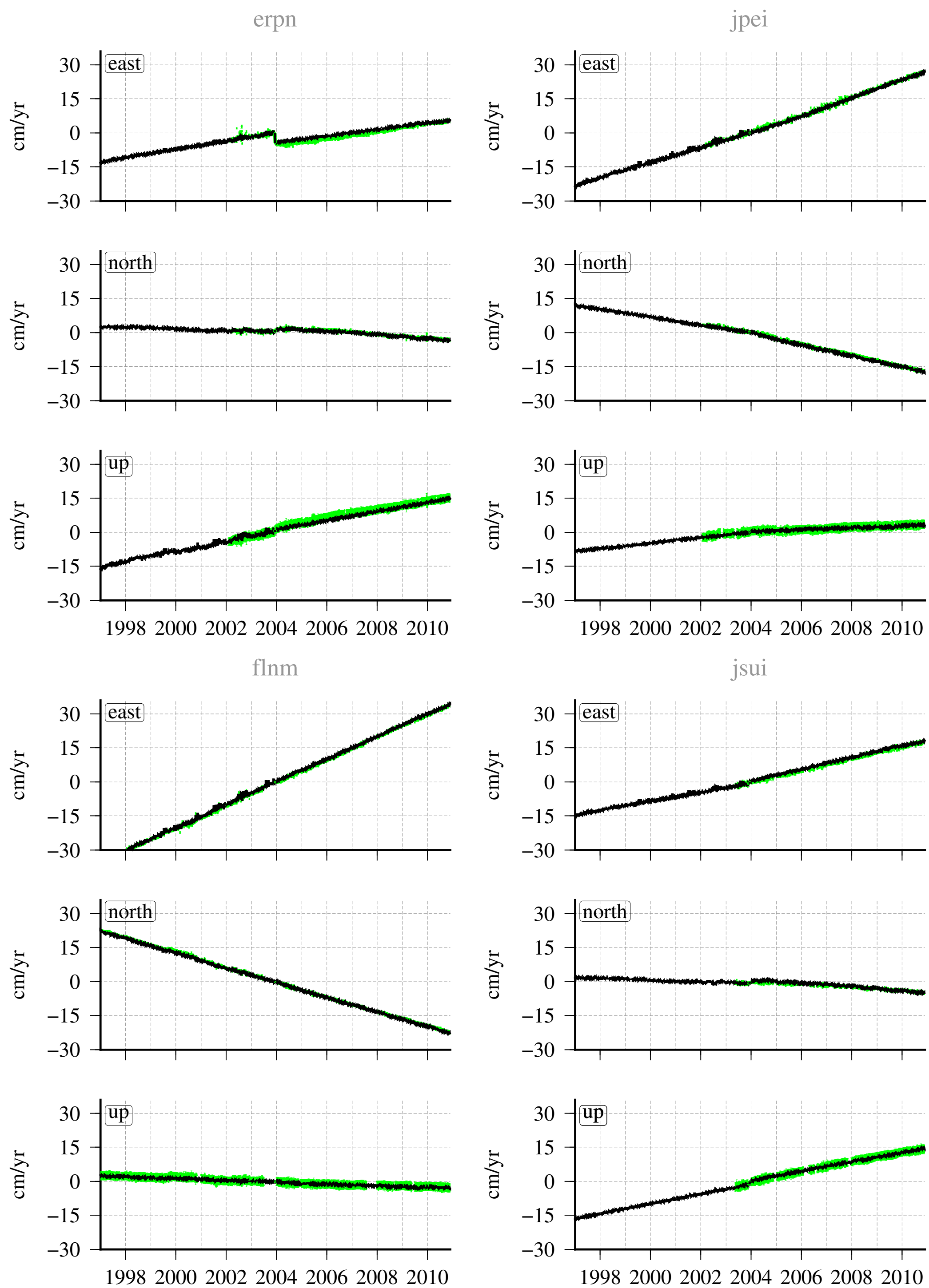
erpn
jpei
flnm
jsui
east
north
up
cm/yr
30
15
0
−15
−30
1998 2000 2002 2004 2006 2008 2010

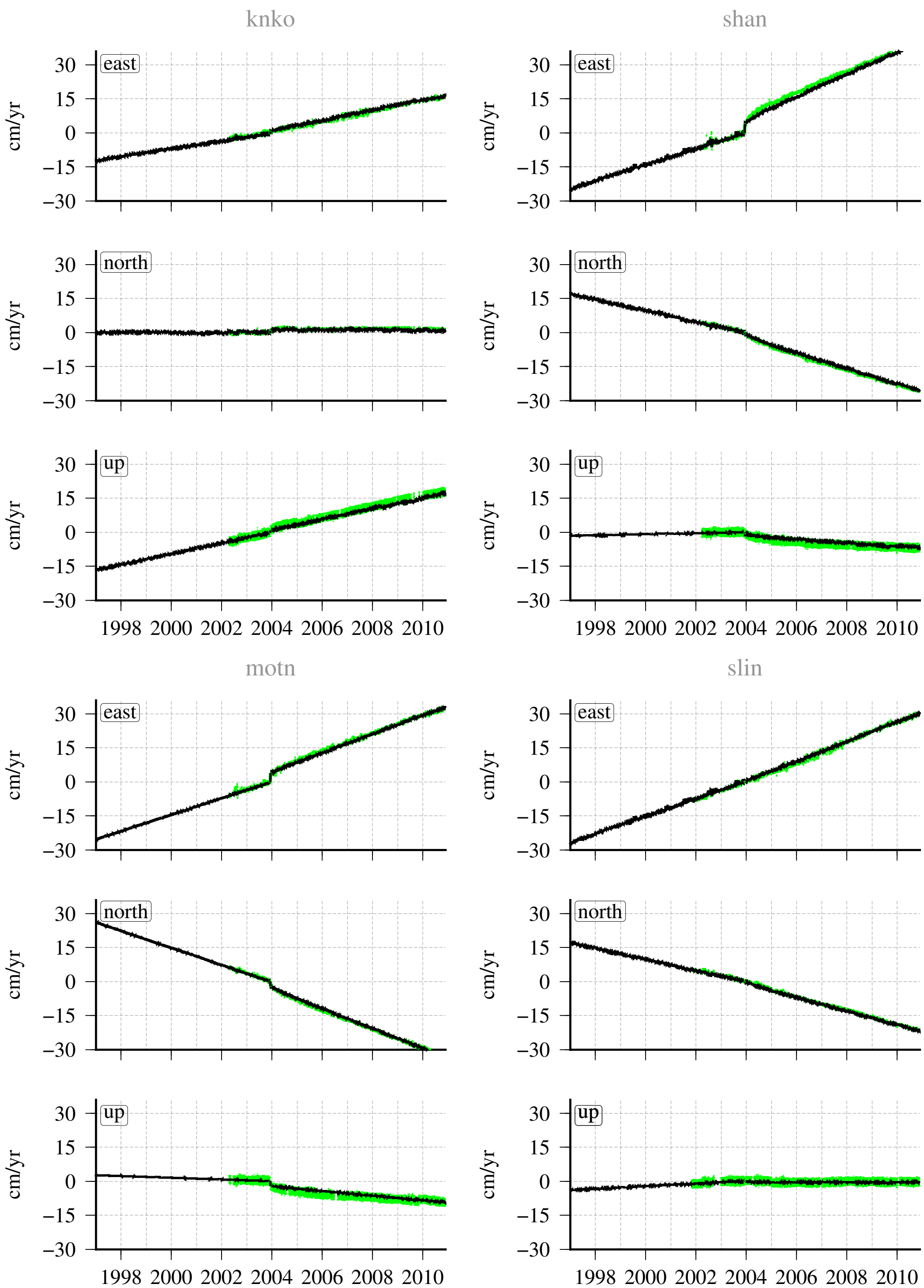
knko
shan
motn
slin
east
north
up
cm/yr
30
15
0
−15
−30
1998
2000
2002
2004
2006
2008
2010

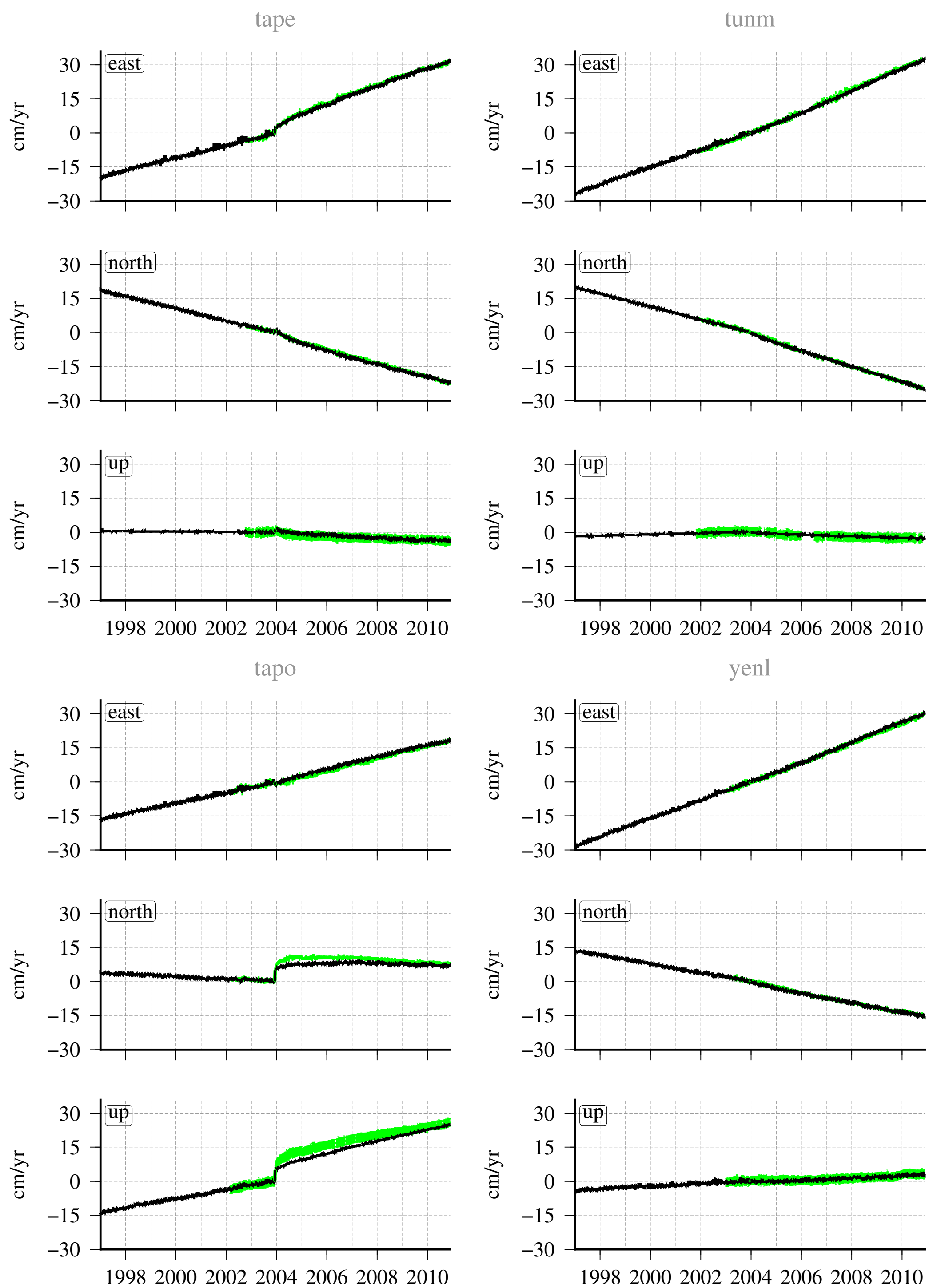
tape
tunm
tapo
yenl
east
north
up
cm/yr
30
15
0
−15
−30
1998 2000 2002 2004 2006 2008 2010

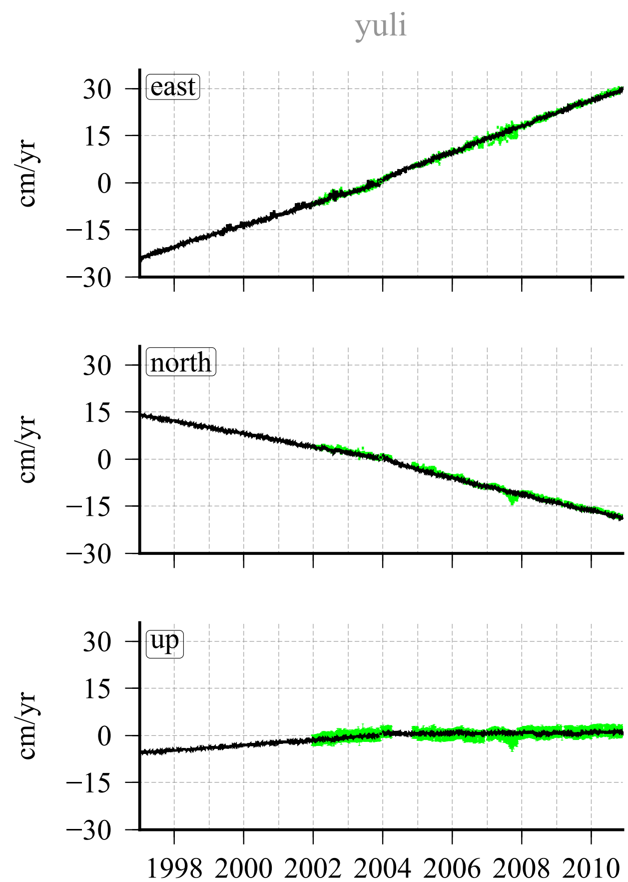

Figure S2: Plots of cGPS times series for which we have records before and after the 2003 Chengkung earthquake. See Figure S1 for location. Green dots with 1-sigma errors bars represents the original dataset. Predictions from the inversion of coseismic slip and PCAIM inversions of preseismic and postseismic periods are plotted in black. To facilitate the comparison we have corrected the model predictions for the mean residual velocities over the pre and post-seismic period represented in Figures 17 and 19.

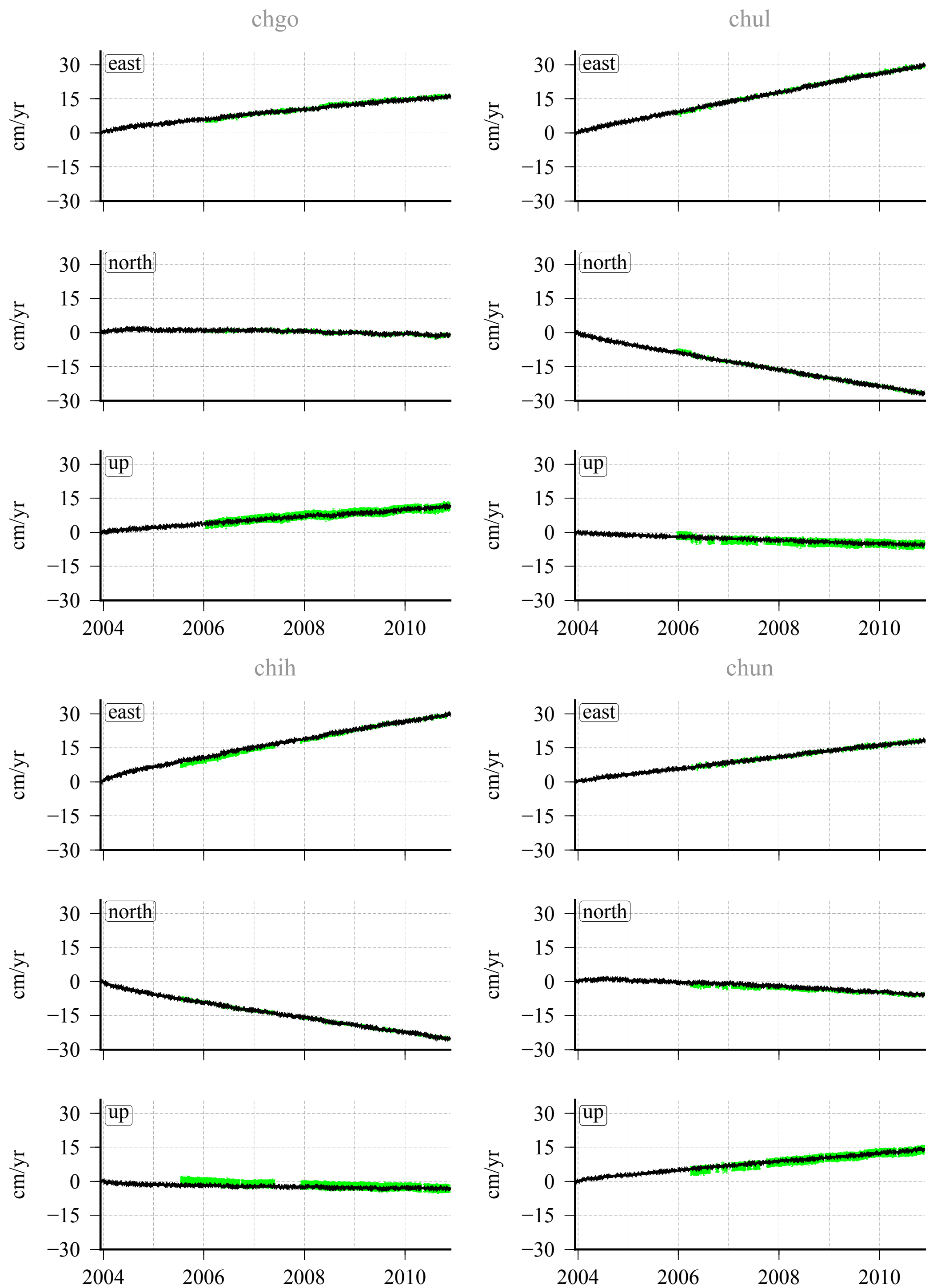
chgo
chul
chih
chun
east
north
up
cm/yr
30
15
0
−15
−30
2004
2006
2008
2010

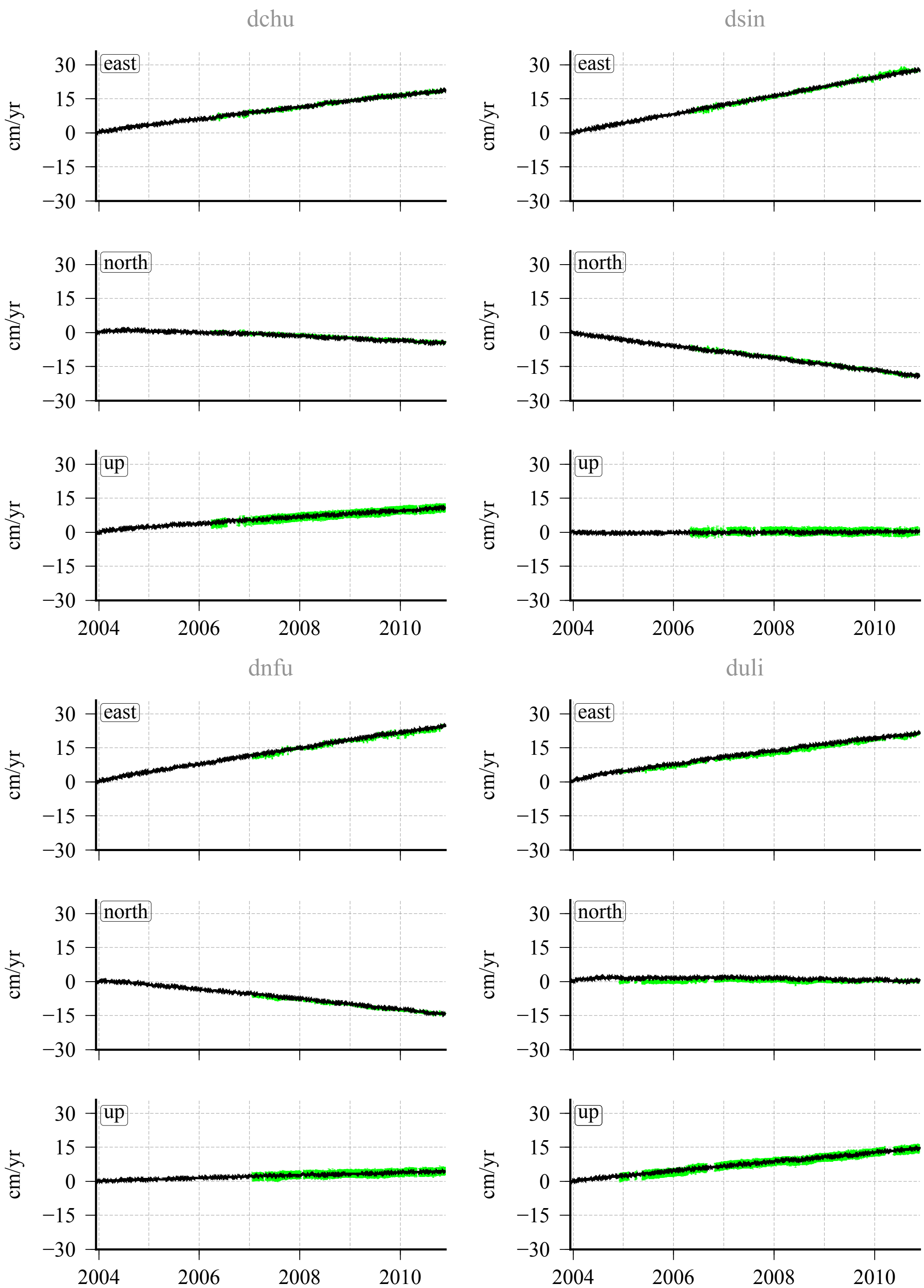

dchu
dsin
dnfu
duli
east
north
up
cm/yr
30
15
0
−15
−30
2004
2006
2008
2010

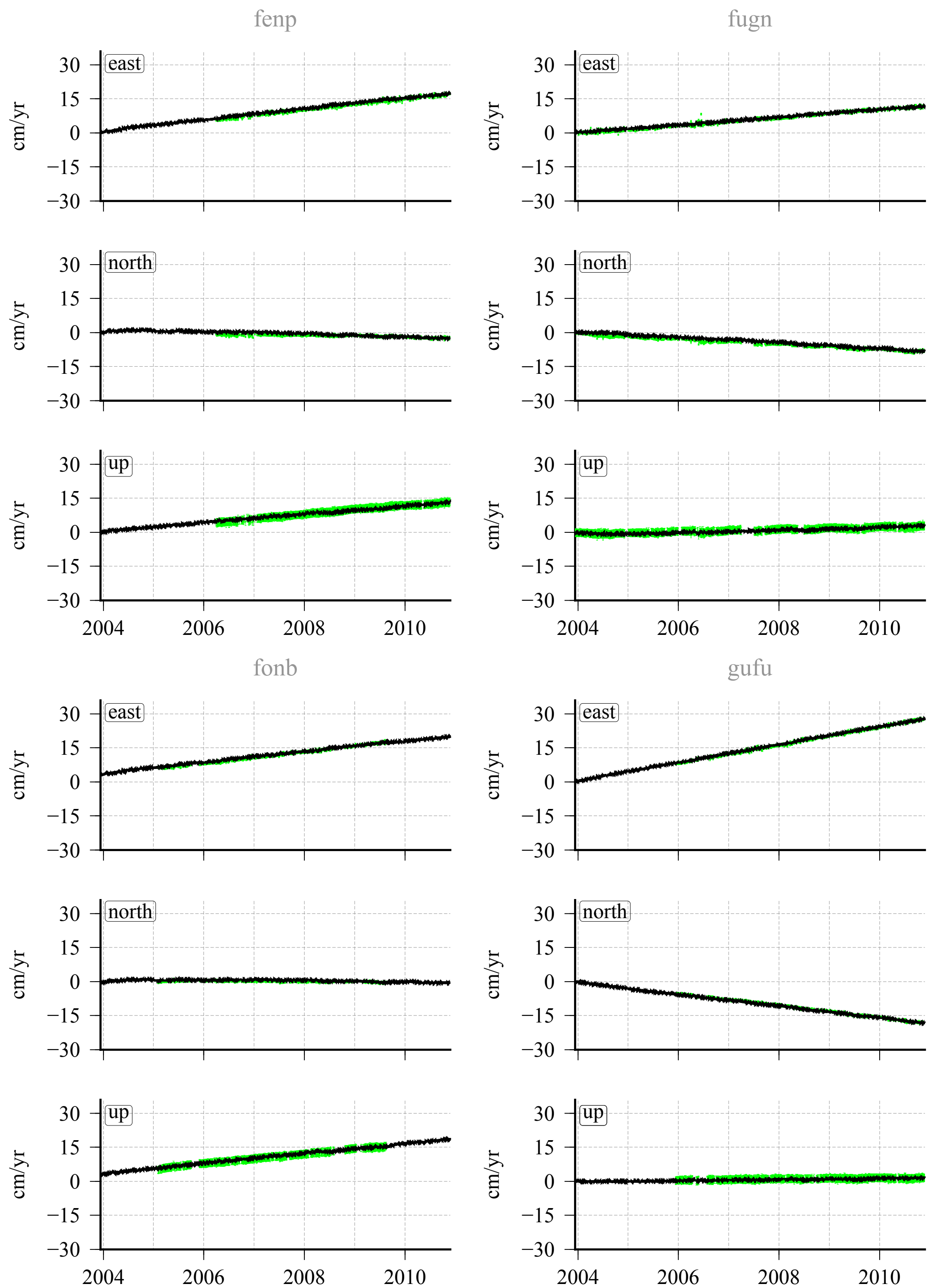
fenp
fugn
fonb
gufu
east
north
up
cm/yr
30
15
0
−15
−30
2004
2006
2008
2010

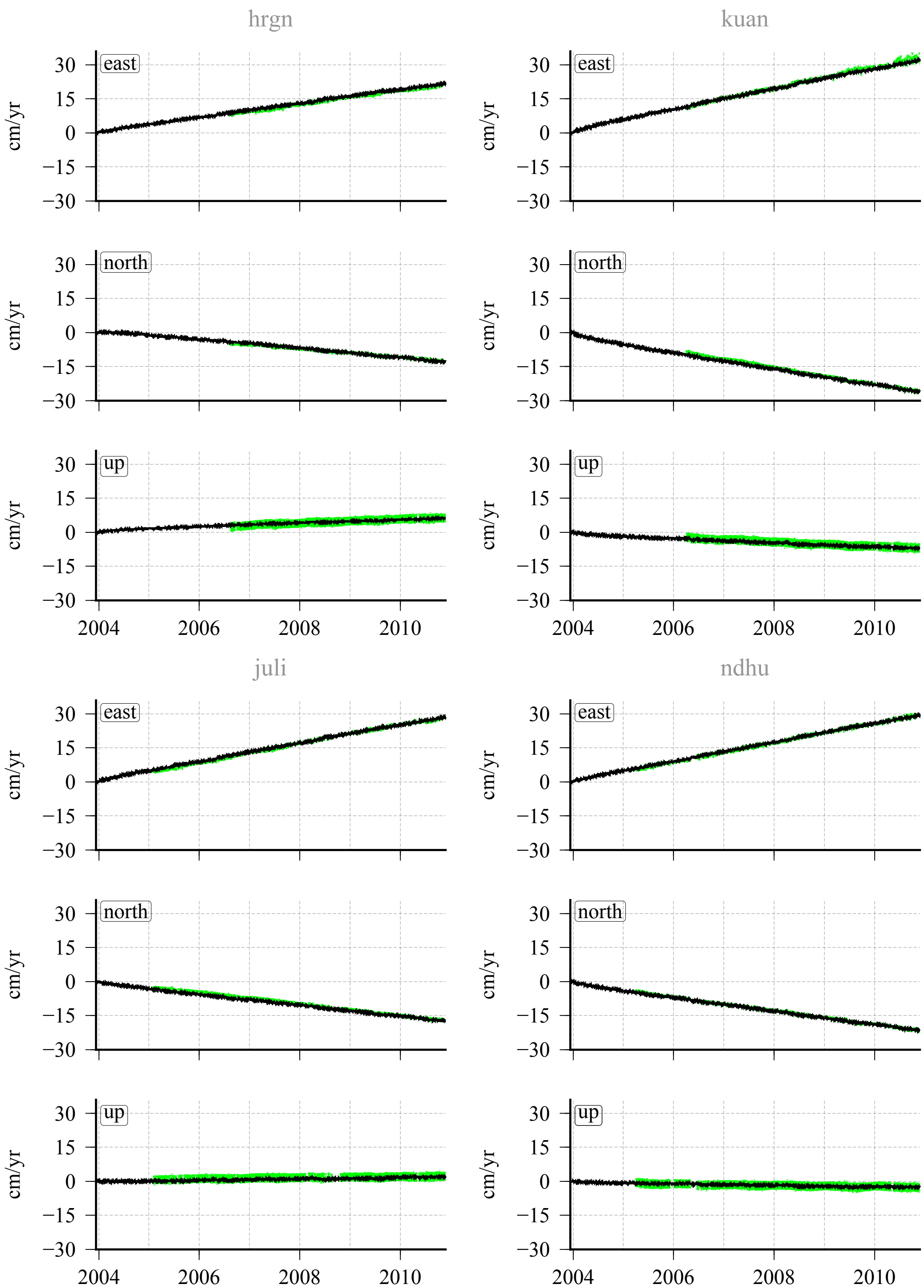
hrgn
kuan
juli
ndhu
east
north
up
cm/yr
30
15
0
−15
−30
2004
2006
2008
2010

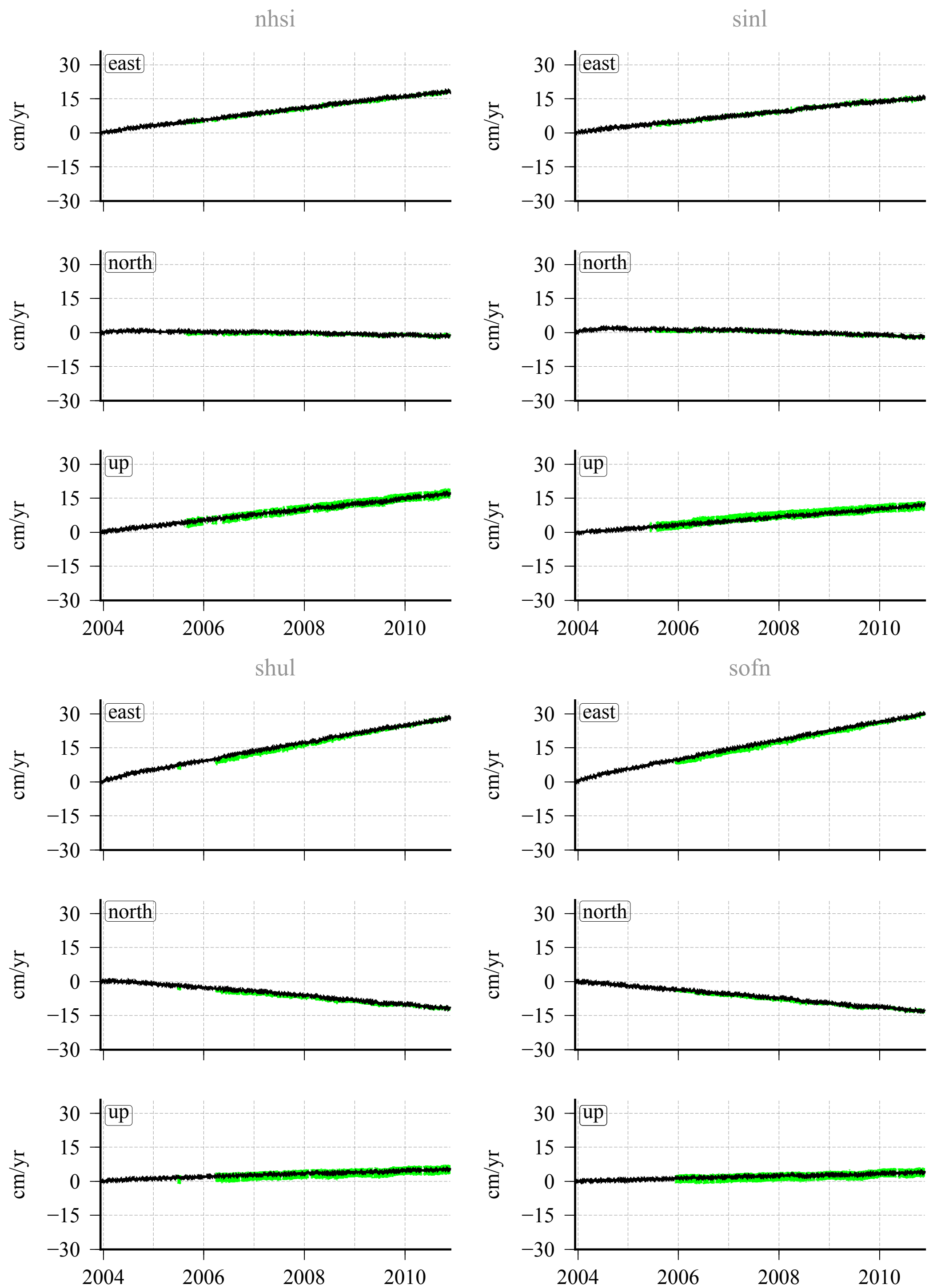
nhsi
sinl
shul
sofn
east
north
up
cm/yr
30
15
0
−15
−30
2004
2006
2008
2010

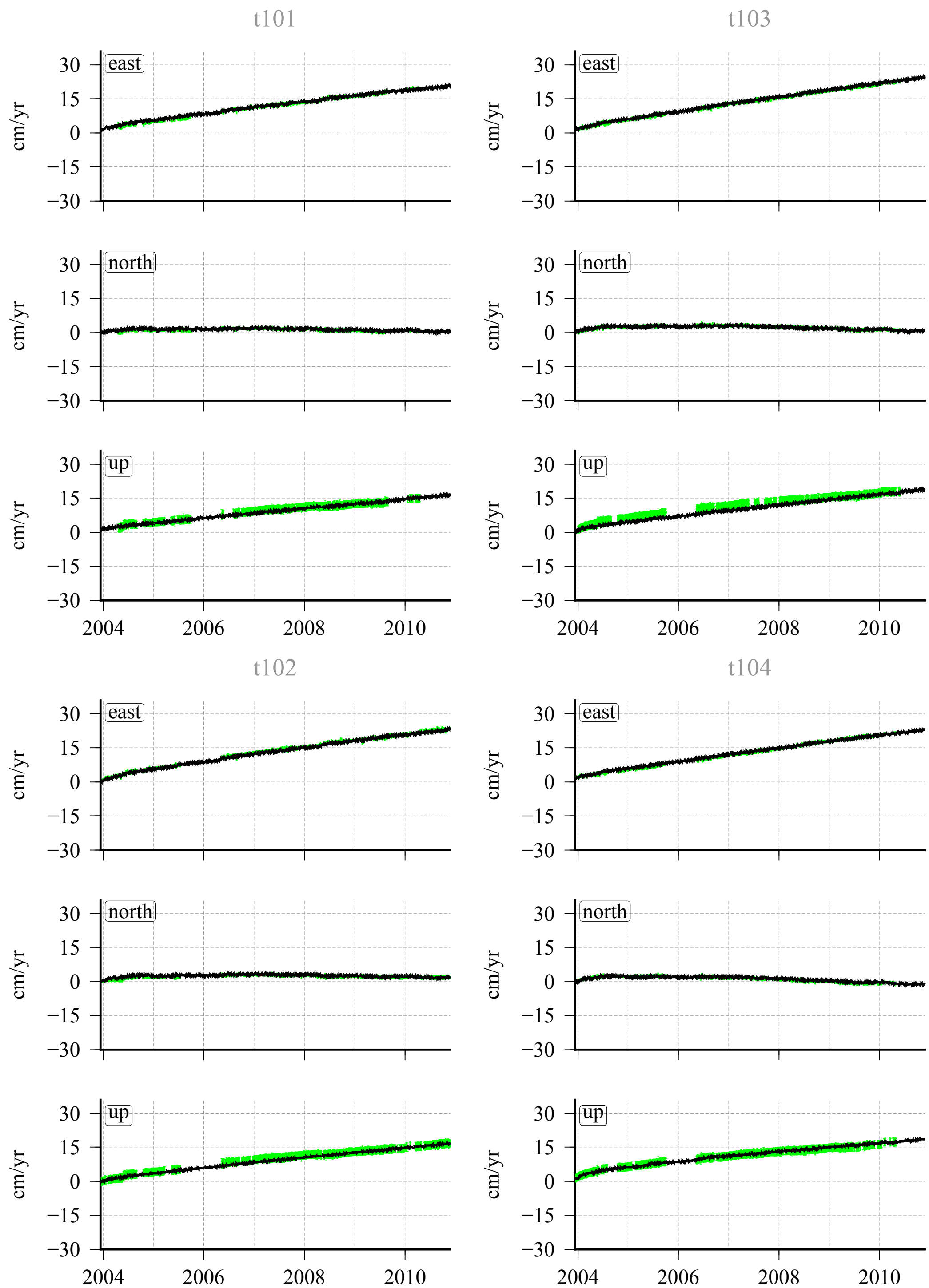
t101
t103
t102
t104
east
north
up
cm/yr
30
15
0
−15
−30
2004
2006
2008
2010

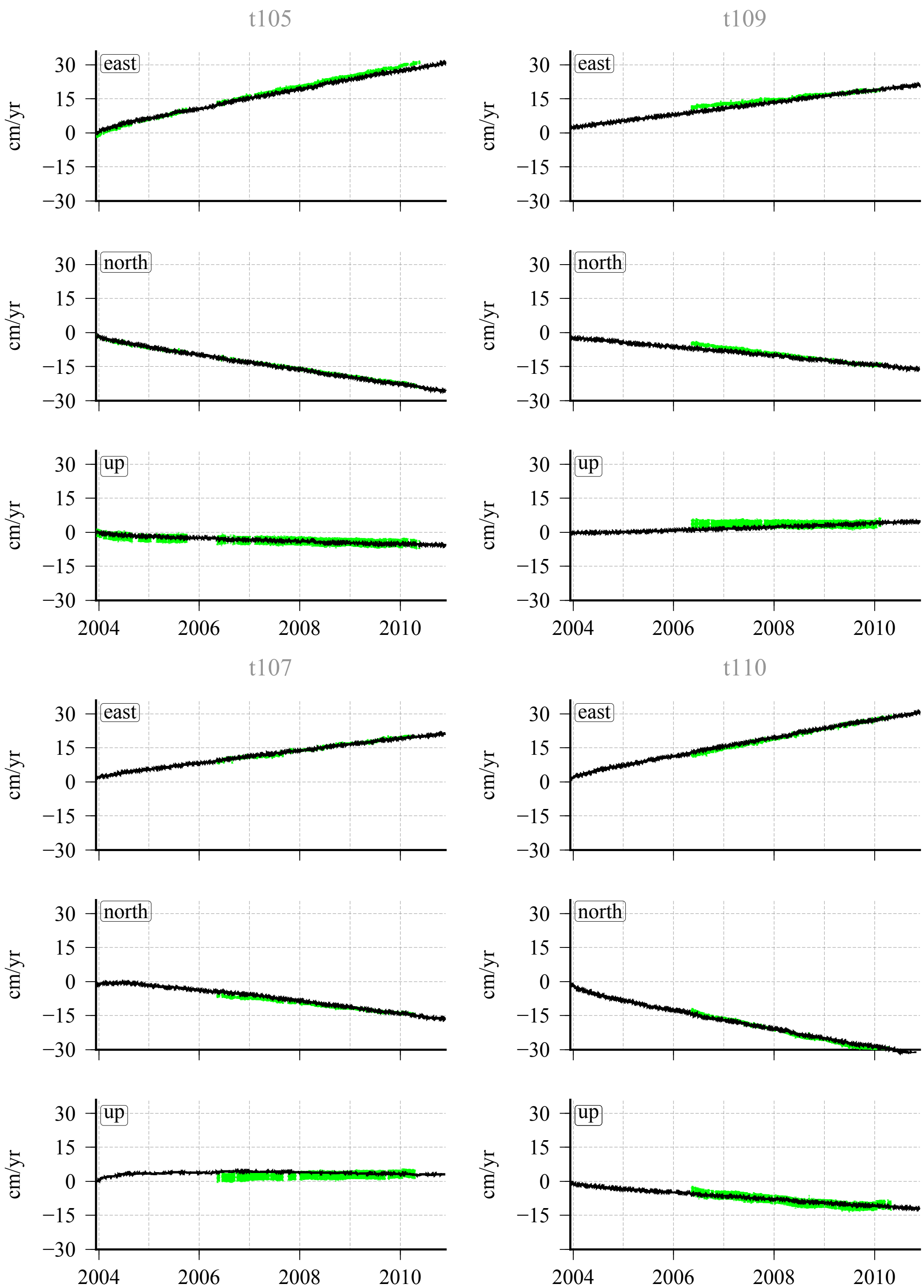
t105
t109
t107
t110
east
north
up
cm/yr
30
15
0
−15
−30
2004
2006
2008
2010

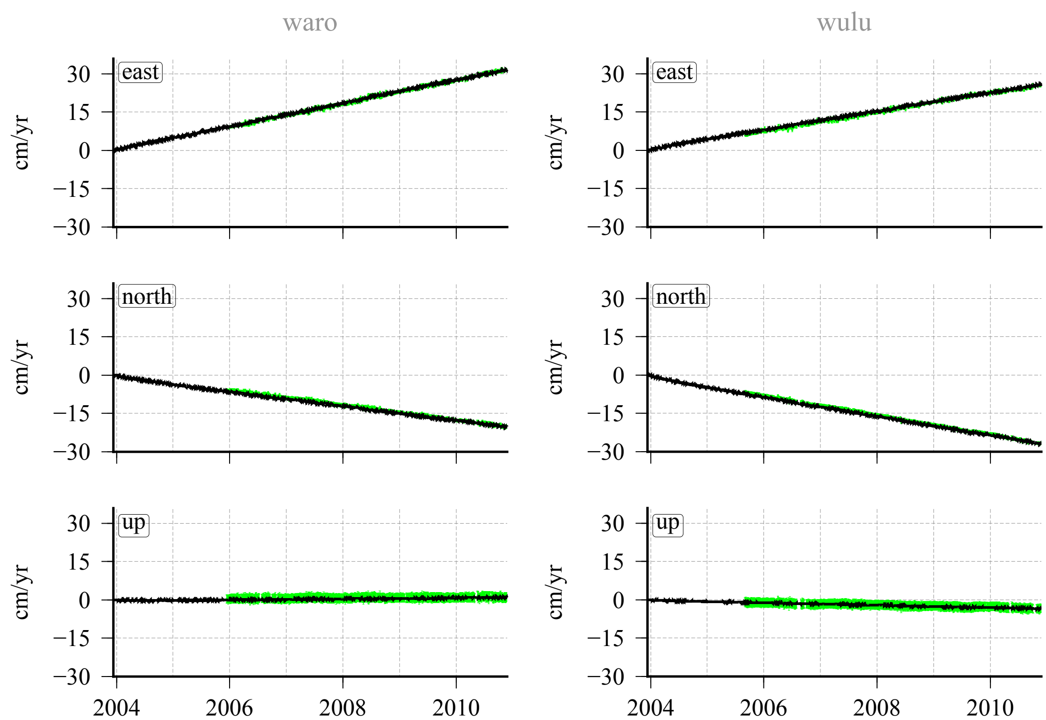

Figure S3: Plots of cGPS times series for which we have records only after the 2003 Chengkung earthquake. See Figure S1 for location. Green dots with 1-sigma errors bars represents the original dataset. Predictions from the inversion of coseismic slip and PCAIM inversions of preseismic and postseismic periods are plotted in black. To facilitate the comparison we have corrected the model predictions for the mean residual velocities over the pre and post-seismic period represented in Figures 17 and 19.

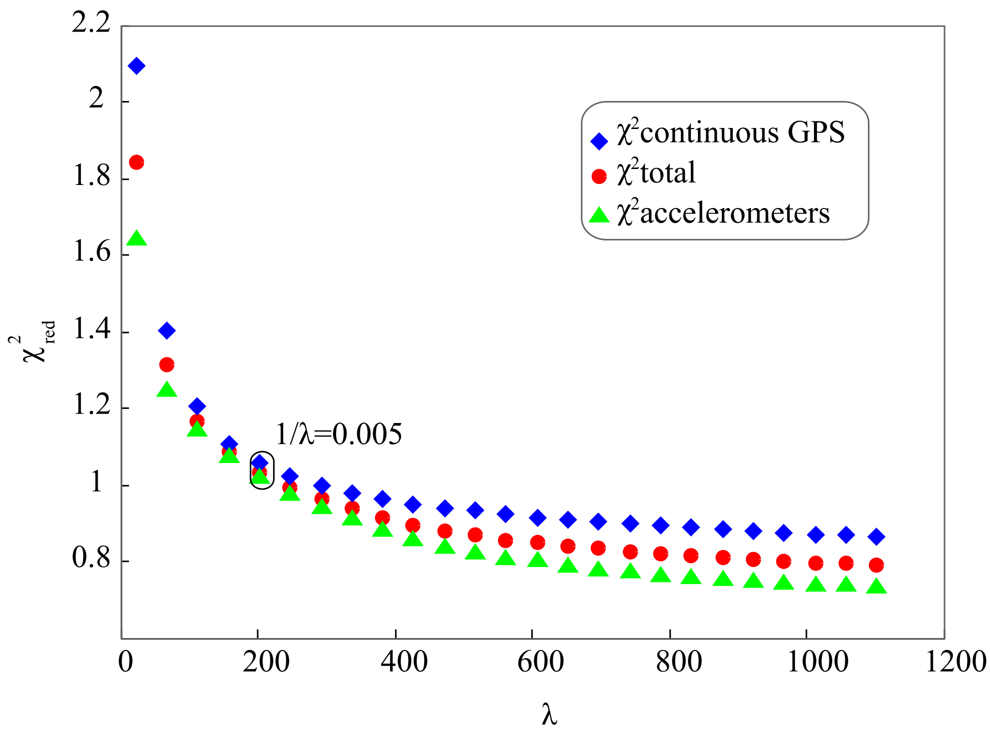

Figure S4: Misfit between measured and reconstructed displacements as the weight put on smoothing (λ) increases. Misfit is quantified from reduced chi-square as defined in equation (4), after renormalization of uncertainties. We choose $1/\lambda = 0.005$ to represent the best compromise.

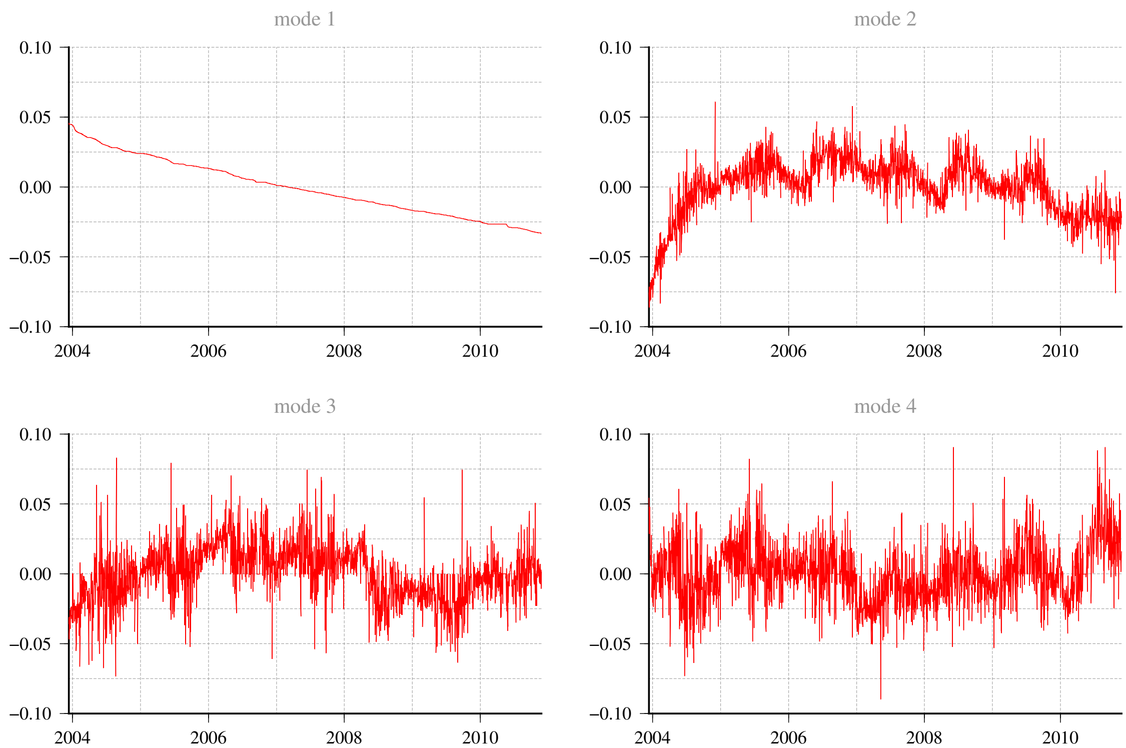

Figure S5: Time functions of the first four principal components for the postseismic modelling. Note that higher-order components (> 2) are more erratic than lower-order components, but do contain significant signals related to postseismic deformation or annual variation of creep rate.

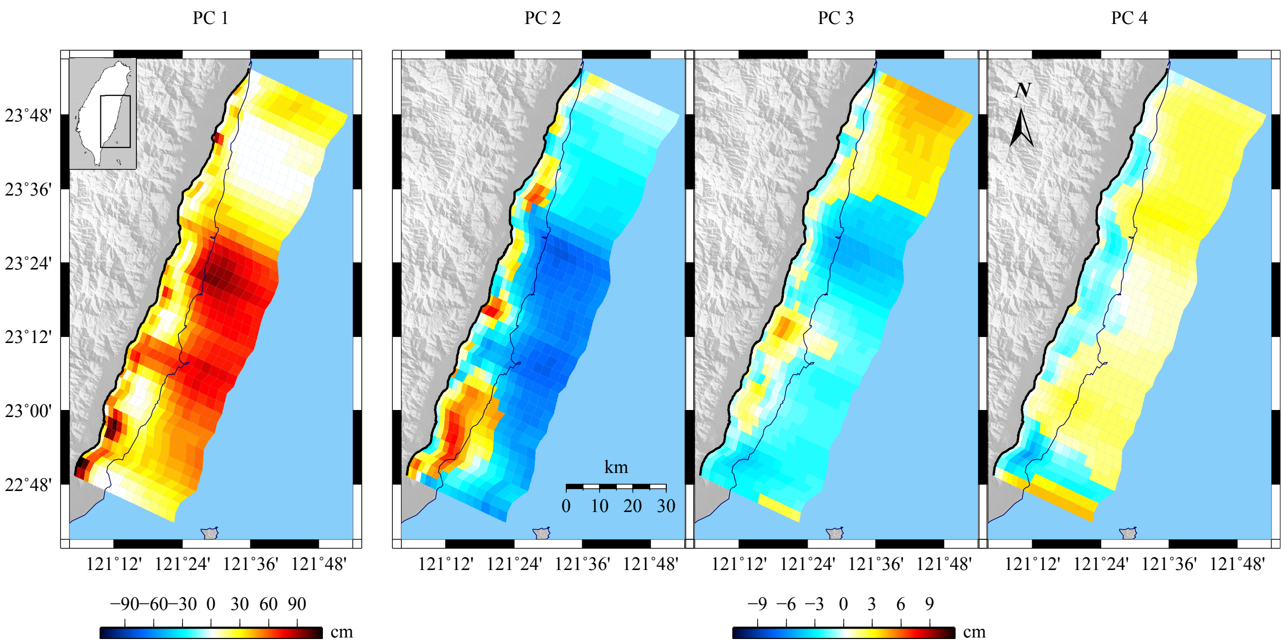

Figure S6: Postseismic principal slip distribution for the four first principal components (PC). Plots display the cumulative slip on the LVF over the period between 12/13/2003 and 11/26/2010, determined from PCAIM inversion of principal components. The range of the color scale is 10 times smaller for PC2, PC3, PC4 than for PC1.

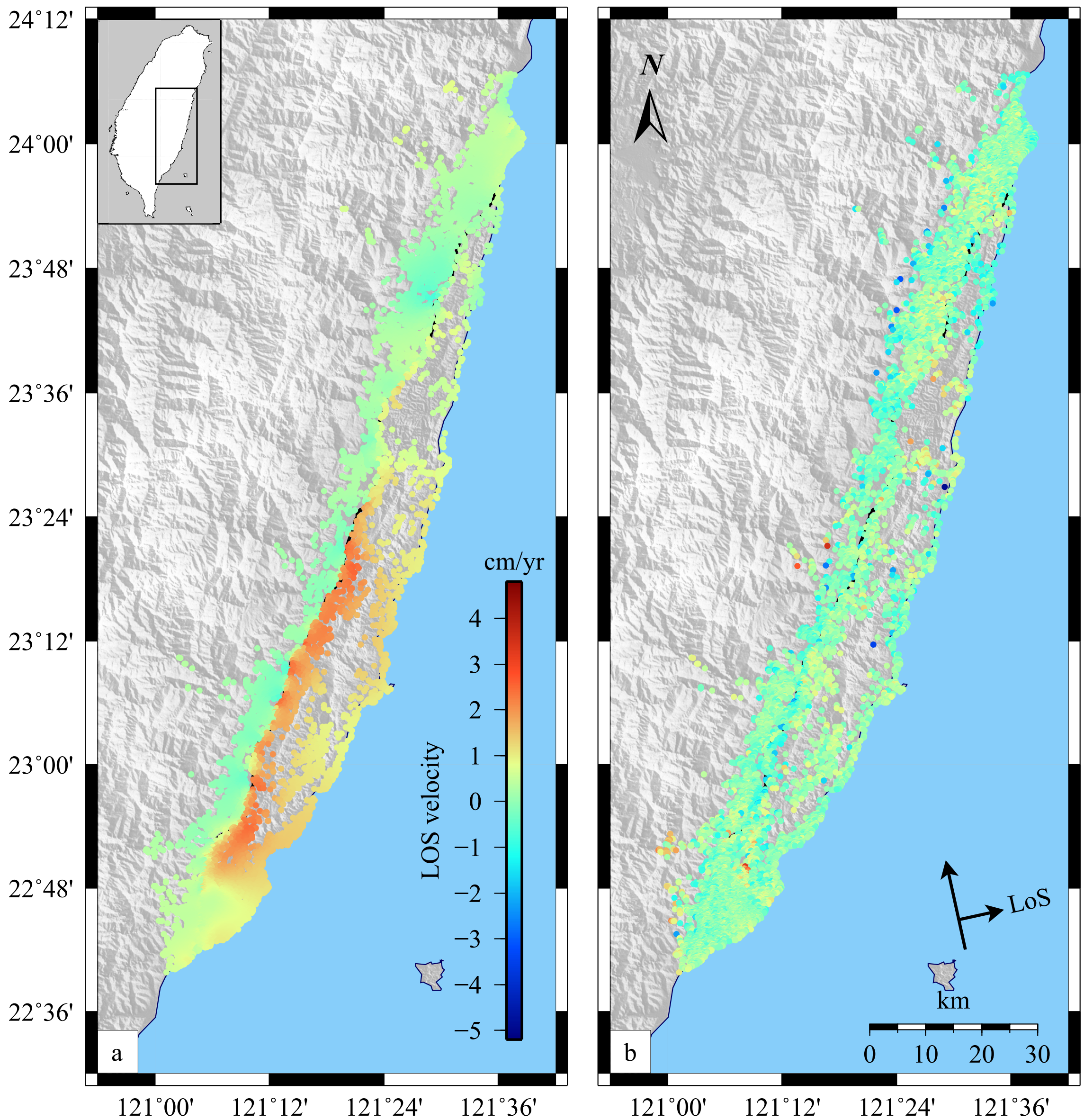

Figure S7: Postseismic model, fit to PS ALOS mean velocity. (a) Line of Sight velocities predicted from the secular interseismic model. For comparison with observations see Figure 2. (b) Residuals from the inversion with same color scale as in (a).

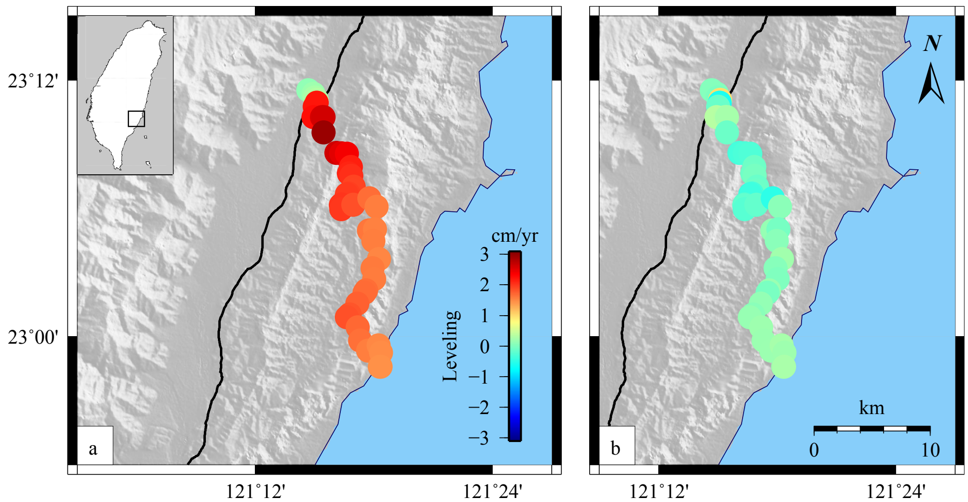

Figure S8: Postseismi model, fit to leveling data. (a) Vertical velocities predicted from the secular interseismic model. See Figure 1 for corresponding observations. (b) Residuals from the inversion with same color scale as in (a).

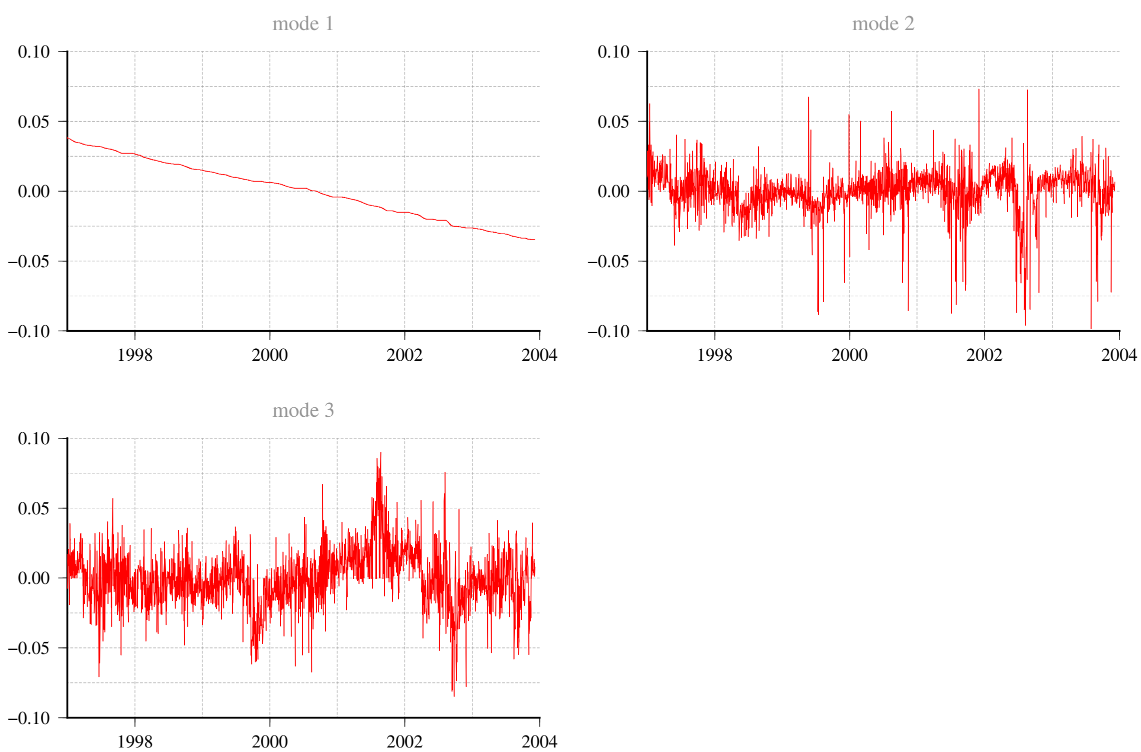

Figure S9: Time functions of the first three principal components for the preseismic modelling.

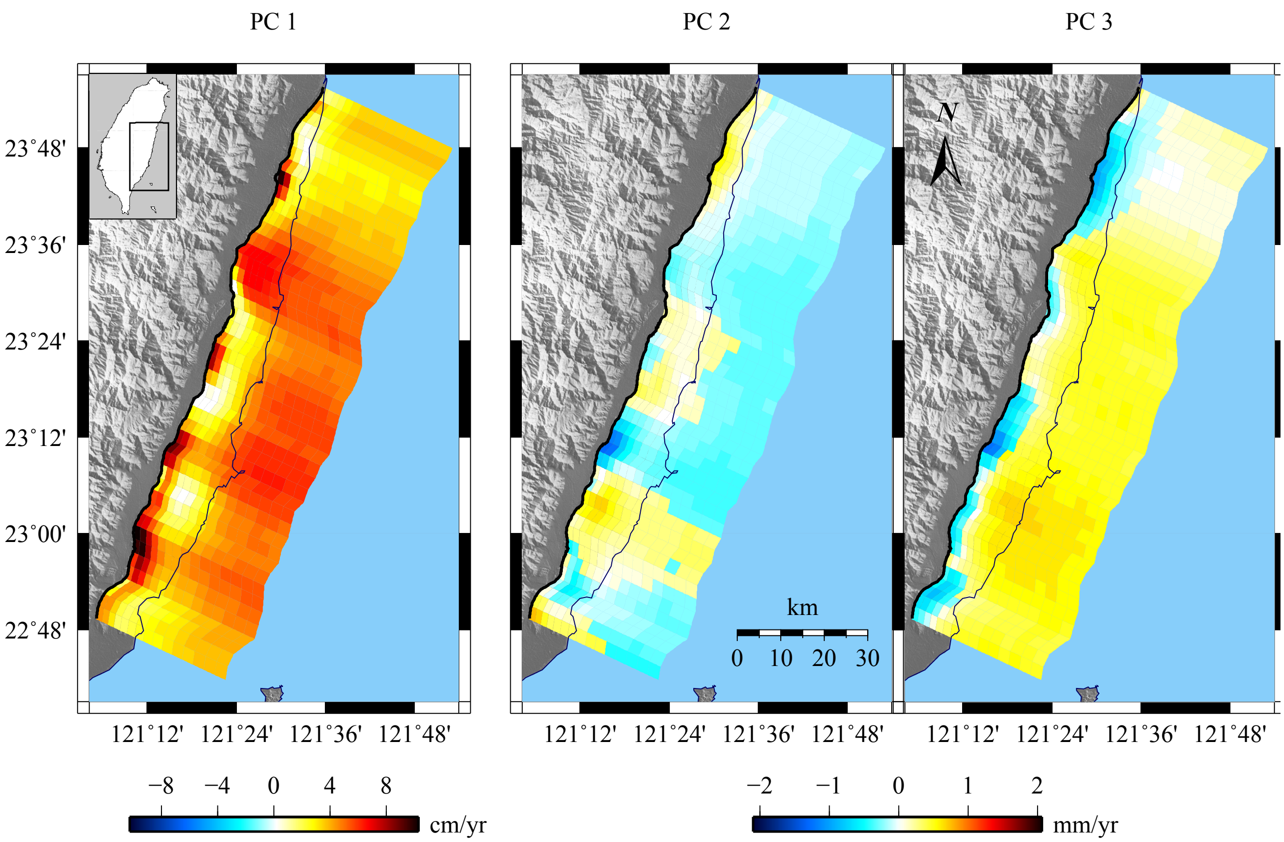

Figure S10: Preseismic principal slip distribution for the three first principal components (PC). Plots display the cumulative slip on the LVF the 1/1/1997 to 12/12/2003 period, determined from PCAIM inversion of principal components. The range of the color scale is 50 times smaller for PC2 and PC3 than for PC1. Therefore most of the slip is accommodated by the first principal component, as comparison with Figure 18a demonstrates.

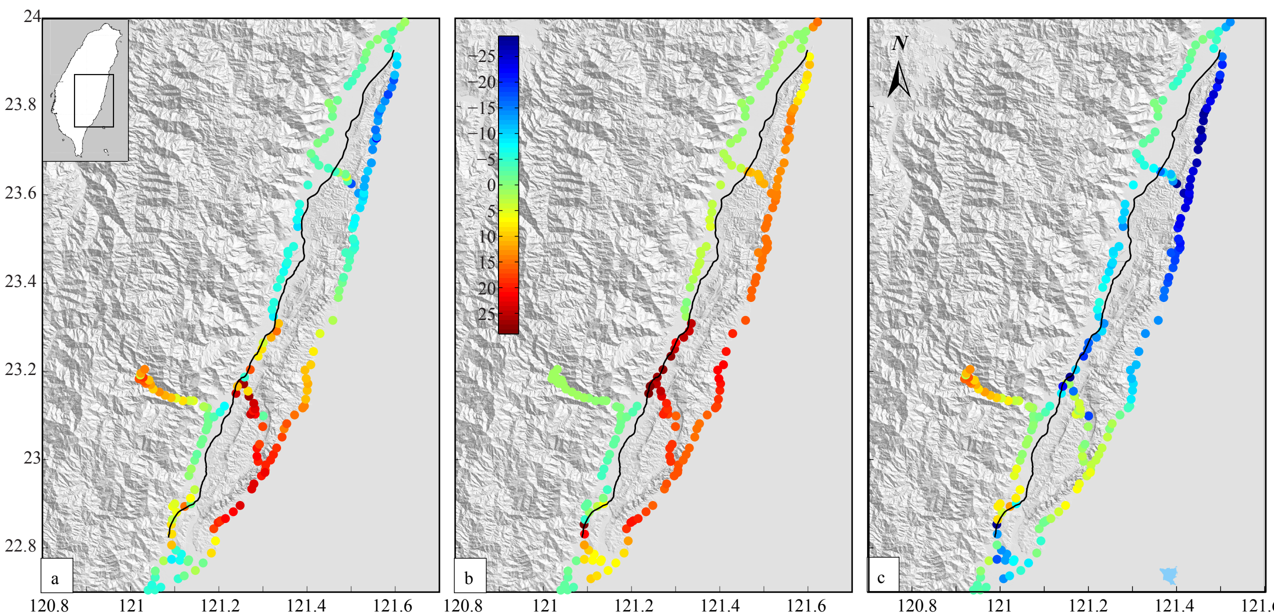

Figure S11: Leveling data from *Ching et al.* (2011).(a) Published Dataset.*Ching et al.* (2011) have removed the coseismic motion due to the chenkung earthquake. Same color scale as in (b). (b) Vertical velocities predicted from the PCAIM preseismic and postseismic models for the same time period.(c) Residuals from the inversion with same color scale as in (a) and (b). Our model does not predicted subsidence in the north, which is linked to Okinawa subduction zone. Residuals in south might be explained by a difference in the coseismic model.

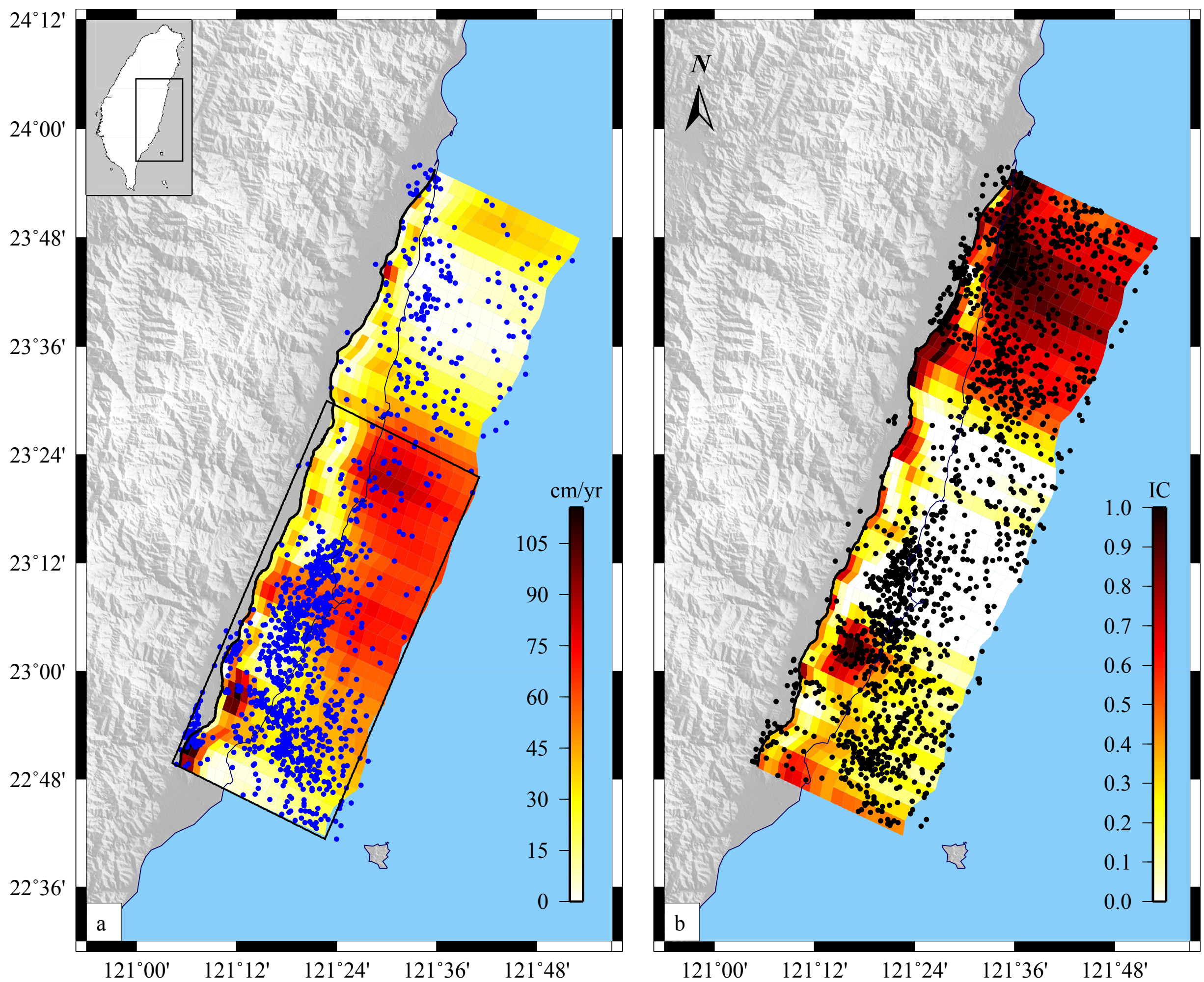

Figure S12: Seismicity around the LVF from 1991 to 2010. (a) Blue dots represents the seismicity recorded on the LVF since the Chengkung earthquake (12/10/2003) until December 2010, for events $M_w > 3$. The black boxe defined the soutern segment of the lVF, for which we compute the Gutenberg-Richter plot (Figure 21). The inversion model underneath corresponds to the cumulative slip on the LVF over the period between 12/11/2003 and 11/26/2010, determined from PCAIM inversion of CGPS and creepmeters time series, leveling data (from 9/1/2007 to 31/20/2010) and PS ALOS cumulative displacement between 1/29/2007 and 6/2/2010. (a) Black dots represents the seismicity recorded on the LVF from January 1991 to the day before the Chenkung earthquake, for events $M_w > 3$. Underneath, we plot the ISC model quantifying the degrees of locking of the LVF fault. If $ISC = 1$, then patch is fully locked, whereas $ISC = 0$ means that the patch is creeping at the long-term slip rate.